DISSERTATIONES
PHYSICAE
UNIVERSITATIS
TARTUENSIS
98

RAUL LAASNER

Excited state dynamics under high excitation densities in tungstates

DISSERTATIONES PHYSICAE UNIVERSITATIS TARTUENSIS
98

DISSERTATIONES PHYSICAE UNIVERSITATIS TARTUENSIS
98

RAUL LAASNER

Excited state dynamics under high excitation densities in tungstates

UNIVERSITY OF TARTU
PRESS
1632

This study was carried out at the Institute of Physics, University of Tartu.

The Dissertation was admitted on June 26, 2015, in partial fulfillment of the requirements for the degree of Doctor of Philosophy in physics, and allowed for defense by the Council of the Institute of Physics, University of Tartu.

Supervisor: Dr. Vitali Nagirnyi, Institute of Physics, University of Tartu, Estonia

Opponent: Dr. Deniss Grjaznovs, Institute for Solid State Physics, University of Latvia, senior researcher

Defense: October 9, 2015, at the University of Tartu, Tartu, Estonia

European Union
European Social Fund

Investing in your future

ISSN 1406-0647
ISBN 978-9949-32-912-0 (print)
ISBN 978-9949-32-913-7 (pdf)

University of Tartu Press
www.tyk.ee

Contents

LIST OF ORIGINAL PUBLICATIONS

This thesis is based on the following publications:

- S. Markov, V. Nagirnyi, A. N. Vasil'ev, V. Makhov, R. Laasner, S. Vielhauer, M. Kirm, R. Grigonis, and V. Sirutkaitis, "Modelling of decay kinetics of self-trapped exciton luminescence in $CdWO_4$ under femtosecond laser excitation in absorption saturation conditions", C. Eur. J. Phys. **10**, 1002 (2012)

  Author's contribution — Partially performed experiments and developed the theoretical model; did full data analysis

- R. Laasner, N. Fedorov, R. Grigonis, S. Guizard, M. Kirm, V. Makhov, S. Markov, V. Nagirnyi, V. Sirutkaitis, A. N. Vasil'ev, S. Vielhauer, and I. A. Tupitsyna, "Band tail absorption saturation in $CdWO_4$ with 100 fs laser pulses", J. Phys.: Condens. Matter **25**, 245901 (2013)

  Author's contribution — Partially performed experiments and developed the theoretical models; did full data analysis; proposed the idea of the nonproportionality model

- R. Laasner, "G_0W_0 band structure of $CdWO_4$", J. Phys.: Condens. Matter **26**, 125503 (2014)

- R. Laasner, V. Nagirnyi, S. Vielhauer, M. Kirm, D. Spassky, V. Sirutkaitis, R. Grigonis, and A. N. Vasil'ev, "Cation influence on exciton localization in homologue scheelites", accepted in J. Phys.: Condens. Matter (2015)

  Author's contribution — Performed most of the experiments; did full data analysis; developed theory.

Chapter 1

INTRODUCTION

This thesis describes the experimental and theoretical investigations of the excited state dynamics under high excitation density conditions of the technologically important tungstate scintillator crystals.

Tungstates have a long history of being used mainly as detectors of ionizing radiation, with applications ranging from medical imaging to astrophysics. For example, $CaWO_4$ (calcium tungstate) is known as the very first scintillator for its use in 1896 for registering x-rays [1] and is still relevant in medical radiography and security systems [2]. Also widely used is $CdWO_4$, which, because of its low afterglow, intense intrinsic luminescence, strong x-ray absorption, and radiation hardness, is suitable for computed tomography [2, 3] and the search for the double-beta decay [4]. Together with $CaWO_4$ and $ZnWO_4$, it is also used for the detection of dark matter [5, 6, 7]. One of the most well-known of the tungstates is $PbWO_4$ for its place in the CMS and ATLAS calorimeters [8]. Recently, $SrWO_4$ and $BaWO_4$, in particular doped with Nd, have found application as Raman laser mediums [9]. In addition, there are currently more than 49 000 airports and 926 seaports in the world that require detectors of contraband nuclear materials for the hindrance of nuclear proliferation [10]. Such detectors often contain elements of tungstate scintillators.

For the development of new efficient scintillators or for improving the efficiency of the current ones, understanding of the their scintillation mechanisms is crucial. One of the major unsolved problems for scintillators is their response nonproportionality to ionizing radiation. The nonproportionality originates from the nonlinear interaction of the excited states and is thus excitation density dependent. Since the density of excitations in the track of an ionizing high-energy particle is randomly distributed for each scintillation event, this leads to a considerable worsening of the energy resolution. Several models have been proposed that, depending on the material, describe the excited state dynamics that lead to nonproportionality [11, 12]. In general, nonproportionality can be modeled by luminescence quenching that is proportional to the 2nd or 3rd power of the density of the excited states in the track or a combination of the two.

Tungstates, which represent the class of excitonic intrinsic scintillators, undergo 2nd order quenching due to the Förster dipole-dipole interaction (FRET) of excitons [12, 13, 14]. In such systems, FRET can be modeled in terms of a bimolecular reaction, where one of the excitons serves as a donor and the other as an acceptor, and as a result one of the excitons recombines nonradiatively while the other ionizes. The rate of the nonradiative transitions is determined by the dipole-dipole interaction radius, $R_{\text{d-d}}$, which is one of the most important parameters for quantifying nonproportionality. A standard technique for determining $R_{\text{d-d}}$ experimentally is measuring the luminescence decay curves under a high excitation density and fitting them to the known models [15, 16]. High excitation densities are required because the density-dependent luminescence quenching, which manifests itself in the modification of the decay curves, is present only for a sufficiently small average distance between the excitons. It is worth noting that the small-radius Frenkel excitons, which are characteristic to the wide band gap tungstate crystals, require much larger excitation densities than the Wannier-Mott excitons for the interaction effects to be noticeable. The possibility of producing such high densities has emerged only during the last decade in the form of novel light sources such as the free electron laser [17] or powerful tunable femtosecond laser systems [14].

A drawback of the current models of dipole-dipole interaction is their sensitivity to the initial density distribution of excitons in the crystal after excitation. The initial distribution is determined by the excitation source intensity profile (e.g., the laser beam profile) and the absorption coefficient. The latter, however, is generally not known in the fundamental absorption region, where most experiments to date have been done, and must be taken from general considerations, which leads to an inaccurate determination of $R_{\text{d-d}}$. An additional complication is the multiplication of electronic excitations, which the current models can only cope with in a rather crude manner. In this work, we take a new approach and study the high density effects by using excitation energies from the band tail region, the so-called Urbach tail [18, 19]. In this region, the absorption coefficient is sufficiently small that it can be either measured directly or accurately extrapolated according to the Urbach law. Additionally, multiplication of electronic excitations is not present in the sub-band-gap region. Doing so allows us to accurately quantify luminescence quenching or nonproportionality, but requires the consideration of an additional effect that is not present in the fundamental absorption region. Namely, we have shown that for a sufficiently high excitation density, excitonic absorption saturates in a way that can be explained by considering the short laser pulse duration and the peculiarities of absorption in the Urbach tail. The saturation induces transparency, which affects the efficiency of dipole-dipole interaction of excitons. We present a new model that combines absorption saturation and dipole-dipole interaction and allows to quantify both effects. The model is successfully applied to the experimental results obtained for $CdWO_4$, $CaWO_4$, and $SrWO_4$.

In order to relate the dipole-dipole interaction radius to the characteristics of the relaxed exciton, we study the time-resolved emission spectra and the temperature dependencies of the intensity and the decay time of the intrinsic emission of $CaWO_4$, $SrWO_4$, and $BaWO_4$. In the series $CaWO_4 \rightarrow SrWO_4 \rightarrow BaWO_4$, we find a correlation between the cation radius, the exciton radius, and the dipole-dipole interaction radius [20]. Due to the similar ground state structural and electronic properties of these crystals, the correlation is shown to be caused by the differences in the excited state dynamics.

Optical experiments, as have been described thus far, provide a fairly controllable environment for studying some aspects of the scintillation mechanism. In practical applications, the crystals are usually irradiated with high-energy particles, which produce a so-called particle track that consists of an inhomogeneous distribution of electronic excitations. We present a model of scintillator nonproportionality, which examines the nonlinear interaction of excitations within the track and is applicable to excitonic scintillators. The model assumes dipole-dipole interaction as the source of nonproportionality and allows experimental nonproportionality data to be fitted to the model for determining the track radius of a high-energy particle.

The track radius could in principle also be calculated from first principles if one correctly accounts for all the processes during thermalization, of which the dominant ones are electron-phonon scattering and electron-electron scattering. Often the thermalization length of hot electrons and holes is estimated by considering only electron-phonon scattering [21]. In this work, we instead calculate only the rates of electron-electron scattering, which allow us to estimate the accuracy of neglecting electron-electron scattering when modeling thermalization. The result will be qualitative in that no transition matrix elements are calculated. Only the rates are calculated, which can be compared to the rates of electron-phonon scattering.

The results presented in this thesis can be divided into three distinct time-scales. *i)* In the excitation stage, which lasts on the order of 100 fs or less, we consider an absorption saturation effect when exciting with fs laser pulses with sub-band-gap energies (Secs. 2.1 and 4.2), or otherwise for a high-energy electron, we present a model for the electron's track (Secs. 2.4 and 4.4). *ii)* In the thermalization stage, which is generally 1–10 ps, we calculate the excited state lifetimes due to electron-electron scattering (Secs. 2.5 and 4.5). *iii)* In the relaxation and luminescence stage, the latter being on the order of 10 µs, we study the dipole-dipole interaction between relaxed excitons (Secs. 2.2, 2.3, 4.1, and 4.3).

1.1 Crystal structure and luminescence properties

Crystal structure. Tungstates are ionic crystals, where the anions are the approximately tetrahedral $WO_4^{\alpha-}$ molecular complexes. The crystals used in this work are $CdWO_4$, $CaWO_4$, $SrWO_4$, and $BaWO_4$, in all of which the cation has a positive charge of close to 2, i.e., $\alpha \approx 2$. Tungstates divide into two categories by crystal structure - wolframites and scheelites. In both cases, there are two formula units of AWO_4 in the unit cell.

$CaWO_4$, $SrWO_4$, and $BaWO_4$ have the scheelite-type structure, which is in the tetragonal class and belongs to the $I4_1/a$ (No. 88) space group. The cation and the W sites have S_4 symmetry, and the crystal has an inversion center. Each W site in these crystals is surrounded by four equivalent O sites at a bond length of approximately 1.8 Å.

$CdWO_4$ has the wolframite-type structure, which is in the monoclinic class and belongs to the $P2/c$ (No. 13) space group. The crystallographic a and c axes intersect at an angle β and are both perpendicular to the b axis. Each W is surrounded by six O sites. The resulting WO_6^{6-} octahedra form a chain by edge sharing, which leads to two inequivalent O sites. Type 1 (O_1) forms a short bond to a W site while type 2 (O_2) has longer bonds to two W sites.

The wolframite structure is a generally more closely-packed structure, naturally forming in materials with small A^{2+} ions while the scheelite structure naturally forms in materials with larger A^{2+} ions [22].

Luminescence mechanism. The crystals used in this work all have a similar electronic structure. The top of the valence band is derived mainly from the O 2p states with some hybridization with the W 5d and the cation states, while the bottom of the conduction band is dominated by the W 5d states [23, 24]. The first excited states are characterized by the formation of an exciton within the WO_4^{2-} molecular ion, followed by significant lattice distortions, resulting in a self-trapped exciton with the hole component localized at O sites and the electron component localized at the W site [25, 26, 23]. The intrinsic emission spectra peak at 2.5–2.9 eV [27, 25, 26]. The Stokes shift is more than 2 eV in all cases (roughly half the excitation energy goes into the Stokes shift). The intrinsic emission of luminescence is based on the radiative recombination of triplet excitons. Due to the forbidden nature of the transitions, the decay time of the unquenched intrinsic luminescence of tungstates is at least 10 μs.

Chapter 2

THEORY

2.1 Absorption saturation with femtosecond pulses in the Urbach tail

In this section, we develop a model of absorption saturation for the excitation stage in the Urbach tail under excitation with femtosecond pulses. The model allows to predict the initial distribution of excitons for the luminescence stage, for which another model is developed in the next section.

Origin of saturation. The Urbach tail refers to the region of energies below the band gap, where phonon-assisted absorption is necessary for excitation. The characteristic exponential energy dependence of the absorption coefficient in the Urbach tail and its variation with temperature has been clearly demonstrated for $CdWO_4$ [28], $ZnWO_4$ [29], and $PbWO_4$ [30] and should be present also in other tungstates.

As the pulse duration gets shorter the phonon formalism ceases to be valid. In the limit of infinitesimally short excitation pulses, phonons should be considered as lattice inhomogeneities [31] and absorption can be described as follows. At the moment of excitation, the absorption probability of a photon with energy $\hbar\omega$ for a given atomic configuration $\boldsymbol{X}$ depends on the availability of excited and ground states $|e,\boldsymbol{X}\rangle$, $|g,\boldsymbol{X}\rangle$ with a suitable displacement from the lattice equilibrium positions providing the energy distance $\hbar\omega$ between these states. Such a single-particle picture describing optical absorption in terms of atomic configurations is an accurate description of the Urbach tail [19]. The absorption probability of the photon can then be expressed as $\propto |V_{eg}|^2\delta(E_e(\boldsymbol{X})-E_g(\boldsymbol{X})-\hbar\omega)$, where V_{eg} is the dipole matrix element and $E_{e(g)}$ is the excited (ground) state energy. Only the centers (lattice sites) with the favorable configuration $\boldsymbol{X}$ for which $E_e(\boldsymbol{X})-E_g(\boldsymbol{X})=\hbar\omega$ holds at the time of excitation can participate in the electronic transition. All such centers have the same absorption cross-section since $|V_{eg}|^2$ depends weakly on the atomic configuration $\boldsymbol{X}$ as the spatial distribution of an electron's wavefunction is much larger compared to an atomic displacement from its equilibrium position. The probability of electronic transition for a given center in the Urbach tail is therefore either a constant or zero and the excitation stage can be approximated with a two-level system.

The limited number of centers capable of absorption during the very short excitation stage (e.g., with fs laser pulses) can lead to absorption saturation. It is interesting to note that if the phonon formalism were valid for fs pulses, then the saturation effect could be explained in terms of the local phonon population being unable to recover during the short time interval.

In wide band gap scintillators, saturated absorption has so far been reported for CsI and NaI crystals [32], where optically induced transparency was described in terms of the dynamic Burstein effect. The latter is caused by the full occupation of the lowest-energy states in the conduction band by nonequilibrium carriers and originates from the Pauli exclusion principle. However, for tungstates, when exciting with sub-band-gap photons, the electrons are excited directly into the exciton band without producing uncorrelated e-h pairs. Excitons are subject to the Bose-Einstein statistics and thus saturation cannot be explained in terms of the Burstein effect as long as the densities are low enough to exclude overlapping of exciton wavefunctions. Since tungstates are characterized by self-trapped excitons (STE) localized at the WO_4^{2-} molecular ions, this requirement is always satisfied.

Absorption saturation in a two-level system. From the rate equations of the two-level system, the absorption coefficient is found to be $\alpha_n = \alpha(1-2n/N)$, where n is the population density of the upper level, N is the maximum population density of the lower level and α is the linear absorption coefficient. In our case, $n \equiv n(\boldsymbol{r},t)$ is the density of electronic excitations and N is the number of centers with the favorable atomic configuration as discussed above. The factor 2 denotes that due to stimulated emission only half of those centers can be excited in the limit. From here on we denote the limit to the density of electronic excitations by $n_0 \equiv N/2$. The excitation stage is then governed by the following differential equations:

$$\begin{aligned}
\frac{\partial n(\rho,\theta,z,t)}{\partial t} &= \alpha\left[1-\frac{n(\rho,\theta,z,t)}{n_0}\right] I(\rho,\theta,z,t), \\
\frac{\partial I(\rho,\theta,z,t)}{\partial z} &= -\alpha\left[1-\frac{n(\rho,\theta,z,t)}{n_0}\right] I(\rho,\theta,z,t), \\
n(\rho,\theta,z,0) &= 0, \\
I(\rho,\theta,0,t) &= I_{\mathrm{P}}(\rho,\theta) f(t),
\end{aligned} \tag{2.1}$$

where $n(\rho,\theta,z,t)$ is the density of electronic excitations, $I(\rho,\theta,z,t)$ is the pulse intensity and $I_{\mathrm{P}}(\rho,\theta)$ and $f(t)$ are the spatial and temporal profiles of the laser beam, respectively. Equations (2.1) show that no absorption occurs at $n = n_0$, which is when the crystal becomes transparent. It follows from the discussion above that the higher the photon energy is in the low-energy tail of excitonic absorption, the smaller the displacements of ions from the lattice equilibrium positions needed to satisfy the conditions of the electronic transition. Therefore, n_0 is expected to increase with increasing excitation energy and, correspondingly, the pulse energies at which the crystal becomes transparent will also be higher. At the excitation energy of resonant exciton creation and above we can formally take $n_0 \to \infty$ (although strictly speaking the closest possible separation of STEs is always limited by the lattice constant). We note that n_0 is also proportional to the pulse energy width and can be different for different experimental setups.

Despite being highly nonlinear, Eqs. (2.1) can be solved to yield (See the Appendix of [16])

$$I(\rho,\theta,z,t) = \frac{I_P(\rho,\theta)f(t)}{1-(1-e^{\alpha z})\exp\left(-\frac{\alpha}{n_0}I_P(\rho,\theta)\int_0^t f(t')\,\mathrm{d}t'\right)} \tag{2.2}$$

and

$$\begin{aligned} n(\rho,\theta,z,t) &= n_0\left[1-\frac{1}{1-e^{-\alpha z}\left(1-e^{F(\rho,\theta,t)}\right)}\right], \\ F(\rho,\theta,t) &= \frac{\alpha}{n_0}I_P(\rho,\theta)\int_0^t f(t')\,\mathrm{d}t'. \end{aligned} \tag{2.3}$$

Equations (2.2) and (2.3) describe the pulse intensity and the density of electronic excitations during the very short excitation stage and are valid for any two-level system regardless of the exact mechanism of saturation.

Direct determination of n_0. The saturation density n_0 can be directly determined from experiment by measuring either the beam intensity profile after transmission or the transmission coefficient if the beam profile before transmission is known.

With a Gaussian spatial beam profile of the form $I_P = I_0\frac{1}{\pi a^2}e^{-\rho^2/a^2}$, where I_0 is the number of photons in the pulse and a is the beam $1/e$ radius, and with *any* temporal beam profile f, Eq. (2.2) yields

$$I(r,z,I_0) = \frac{n_0}{\alpha}\ln\left[\left(\exp\left(\frac{\alpha}{n_0}\frac{I_0}{\pi a^2}e^{-r^2/a^2}\right)-1\right)e^{-\alpha z}+1\right] \tag{2.4}$$

for the beam intensity distribution and

$$T(z,I_0) = \frac{n_0\pi a^2}{I_0\alpha}\int_0^{\frac{I_0\alpha}{n_0\pi a^2}}\frac{\mathrm{d}x}{x}\ln\left[(e^x-1)e^{-\alpha z}+1\right] \tag{2.5}$$

for the transmission coefficient. Here z is the sample thickness.

A measurement of I or T with a fit to Eq. (2.4) or (2.5) could in principle be achieved with thin films of the crystals. For this purpose, we have grown thin

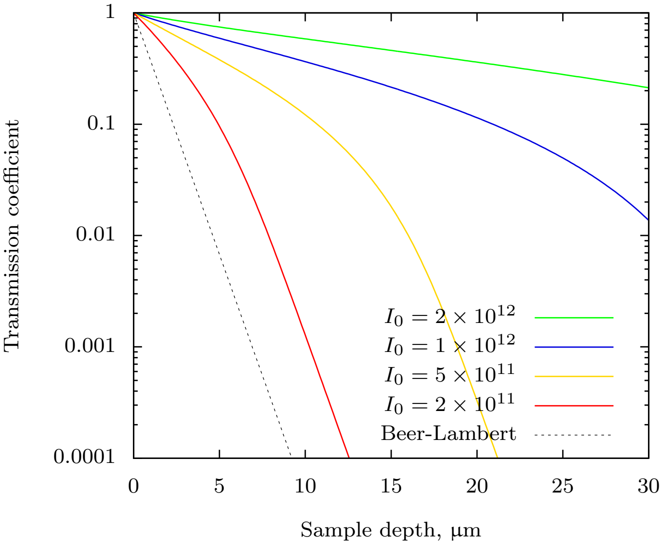

Figure 2.1: Transmission of a thin crystal with the model parameters $n_0 = 10^{19}\,\mathrm{cm}^{-3}$, $\alpha = 10^4\,\mathrm{cm}^{-1}$, $a = 30\,\mu\mathrm{m}$.

films of $CdWO_4$ deposited on MgO and CaF_2 crystals. However, due to a complex influence of the substrate material and some technical difficulties, we were unable to perform the measurements with satisfactory accuracy and may only provide some modeling results with (2.4) and (2.5).

Figure 2.1 shows the behavior of the transmission coefficient for various pulse intensities for a model system. It is seen that the higher the pulse intensity, the more transparent the sample becomes. The saturation effect would also be noticeable by varying I_0 instead of z.

Figure 2.2 shows the variation in the shape of the pulse profile after transmission. Since the saturation effect is greatest at regions of maximum excitation density, the effective absorption coefficient becomes smaller at points closer to the beam symmetry axis. The shape of the beam profile is thus expected to become narrower with increasing pulse intensity. Starting at a certain intensity, however, it starts widening again since in the limit of infinite pulse intensities, the crystal is almost completely transparent and there is no change in the beam profile.

Indirect determination of n_0. Indirect determination of n_0 refers to observing the effects of saturation during the later stages of the scintillation process. Specifically, in tungstates, the saturation effect, which takes place during the short excitation stage, influences the luminescence stage, where the rate of luminescence quenching is dependent on the initial distribution of excitations.

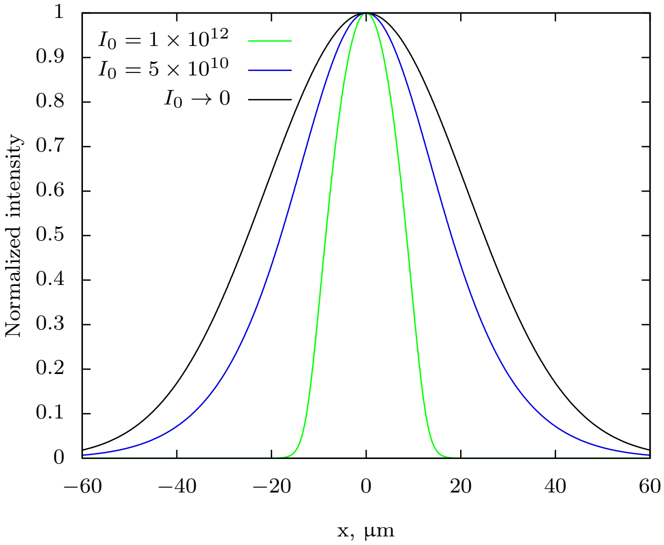

Figure 2.2: Beam profile after transmission at various pulse intensities. The model parameters are $n_0 = 10^{19}\,\mathrm{cm}^{-3}$, $\alpha = 10^4\,\mathrm{cm}^{-1}$, $a = 30\,\mu\mathrm{m}$, $z = 30\,\mu\mathrm{m}$.

With a suitable model for the luminescence intensity that uses Eq. (2.3) as the initial condition for the density of excitations, n_0 could be determined by fitting the luminescence decay curves to the model. The derivation of such a model is presented in the next section.

2.2 Dipole-dipole interaction of excitons

In general, the luminescence stage is a competition between radiative and nonradiative transitions to the ground state involving uncorrelated electrons and holes, different types of defects, and excitons. For the undoped single crystals used in this work, we can consider only radiative transitions due to exciton recombination and nonradiative transitions due to the dipole-dipole interaction of excitons. The rate equation for the exciton density during the luminescence stage is then

$$\frac{\partial n(\boldsymbol{r},t)}{\partial t} = D\nabla^2 n(\boldsymbol{r},t) - \frac{n(\boldsymbol{r},t)}{\tau} - k_2(\boldsymbol{r},t)n^2(\boldsymbol{r},t), \tag{2.6}$$

where n is the exciton density, D is the diffusion coefficient, τ is the radiative decay time, and k_2 is the bimolecular rate constant. In this work, the experiments are performed at temperatures below the onset of thermal quenching of STEs, which allows to neglect the diffusion term, i.e., we shall use the approximation of immobile excitons.

According to the theory of the Förster resonance energy transfer between electric dipoles (FRET), the probability of an STE + STE $\to$ 0 type of reaction is

$$w(r) = \frac{1}{\tau}\left(\frac{R_{\text{d-d}}}{r}\right)^6, \tag{2.7}$$

where r is the distance between two excitons and $R_{\text{d-d}}$ is the characteristic dipole-dipole interaction radius. The bimolecular rate constant is then given by [15]

$$k_2(t) = \frac{2\pi^{3/2}}{3}\frac{R_{\text{d-d}}^3}{\sqrt{\tau t}}. \tag{2.8}$$

Inserting Eq. (2.8) into Eq. (2.6) yields the solution

$$n(\boldsymbol{r},t) = \frac{N_0(\boldsymbol{r})e^{-t/\tau}}{1+\frac{2}{3}\pi^2 R_{\text{d-d}}^3 N_0(\boldsymbol{r})\,\text{erf}\left(\sqrt{t/\tau}\right)}, \tag{2.9}$$

where N_0 is the initial distribution of excitons and erf is the error function. Taking into account absorption saturation during the excitation stage, N_0 is given by $n(\rho,\theta,z,t=T)$ [Eq. (2.3)], where T is the laser pulse duration. Such a substitution is justified if the stages of excitation and luminescence take place in different times scales, making Eqs. (2.1) and (2.6) uncoupled. This holds for $CdWO_4$, where STE relaxation lasts for picoseconds [33], and is presumably true also for other tungstates. The luminescence intensity is given by

$$I_{\text{lum}}(t) = \frac{2\pi}{\tau}\int_0^{z_0}\mathrm{d}z\int_0^{\infty}\rho\,\mathrm{d}\rho\,\frac{n(\rho,\theta,z,T)e^{-t/\tau}}{1+\frac{2}{3}\pi^2 R_{\text{d-d}}^3 n(\rho,\theta,z,T)\,\text{erf}\left(\sqrt{t/\tau}\right)}, \tag{2.10}$$

where z_0 is the sample thickness. We shall consider two explicit forms for n in Eq. (2.10) - one based on a Gaussian laser beam profile and one based on a uniform beam profile.

For a Gaussian beam profile, we insert $I_{\text{P}} = I_0\frac{1}{\pi a^2}e^{-\rho^2/a^2}$ into Eq. (2.3), where I_0 and a have the same meaning as in Eq. (2.4). Note that $\int_0^T f(t)\,\mathrm{d}t = 1$ for any temporal profile. Equation (2.10) then yields

$$\begin{aligned} I_{\text{lum}}(t) =& \frac{n_0\pi a^2}{\tau\alpha(1+c(t))}e^{-t/\tau}\int_0^{\frac{I_0\alpha}{n_0\pi a^2}}\frac{\mathrm{d}x}{x}\ln\left[\frac{(e^x-1)(1+c(t))+1}{(e^x-1)(1+c(t))e^{-\alpha z_0}+1}\right], \\ c(t) =& \frac{2}{3}\pi^2 n_0 R_{\text{d-d}}^3\,\text{erf}\left(\sqrt{t/\tau}\right). \end{aligned} \tag{2.11}$$

This result is valid for any absorption and sample thickness (including, e.g., thin films). However, for $\alpha z_0 \gg 1$ (single crystals and/or strong absorption) Eq. (2.11) reduces to

$$I_{\text{lum}}(t) = \frac{n_0\pi a^2}{\tau\alpha} e^{-t/\tau} \int_0^{\frac{I_0\alpha}{n_0\pi a^2}} \mathrm{d}x \\ \times \frac{\ln\left[(e^x-1)\left(1+\frac{2}{3}\pi^2 n_0 R_{\text{d-d}}^3 \operatorname{erf}\left(\sqrt{t/\tau}\right)\right)+1\right]}{x\left(1+\frac{2}{3}\pi^2 n_0 R_{\text{d-d}}^3 \operatorname{erf}\left(\sqrt{t/\tau}\right)\right)}. \quad (2.12)$$

We remind that the model of absorption saturation is valid only in the band tail region. In the fundamental absorption region we may formally take $n_0 \to \infty$, in which case Eq. (2.12) reduces to

$$I_{\text{lum}}(t) = \frac{I_0}{\tau} e^{-t/\tau} \frac{-\operatorname{Li}_2\left(-\frac{2}{3}I_0\frac{\pi\alpha}{a^2}R_{\text{d-d}}^3 \operatorname{erf}\left(\sqrt{t/\tau}\right)\right)}{\frac{2}{3}I_0\frac{\pi\alpha}{a^2}R_{\text{d-d}}^3 \operatorname{erf}\left(\sqrt{t/\tau}\right)}, \quad (2.13)$$

which is what has been used in the previous studies of the nonlinear quenching of exciton luminescence [13, 14, 17, 32].

For uniform excitation we take $I_{\text{P}} = I_0/\Delta S$ in Eq. (2.3), where ΔS is the area of excitation. Equation (2.10) then yields

$$I_{\text{lum}}(t) = \frac{\Delta S n_0}{\tau\alpha(1+c(t))} e^{-t/\tau} \ln\left[\frac{\left(\exp\left(\frac{I_0\alpha}{\Delta S n_0}\right)-1\right)(1+c(t))+1}{\left(\exp\left(\frac{I_0\alpha}{\Delta S n_0}\right)-1\right)(1+c(t))e^{-\alpha z_0}+1}\right], \quad (2.14)$$

which for $\alpha z_0 \gg 1$ becomes

$$I_{\text{lum}}(t) = \frac{\Delta S n_0}{\tau\alpha} e^{-t/\tau} \frac{\ln\left[\left(\exp\left(\frac{I_0\alpha}{\Delta S n_0}\right)-1\right)(1+c(t))+1\right]}{1+c(t)}, \quad (2.15)$$

which in turn for $n_0 \to \infty$ becomes

$$I_{\text{lum}}(t) = \frac{I_0}{\tau} e^{-t/\tau} \frac{\ln\left[1+\frac{2}{3}\pi^2\frac{I_0\alpha}{\Delta S}R_{\text{d-d}}^3 \operatorname{erf}\left(\sqrt{t/\tau}\right)\right]}{\frac{2}{3}\pi^2\frac{I_0\alpha}{\Delta S}R_{\text{d-d}}^3 \operatorname{erf}\left(\sqrt{t/\tau}\right)}, \quad (2.16)$$

which is Eq. 20 from [15].

Data analysis. Any of Eqs. (2.11)–(2.16), depending on the beam profile and excitation energy, may be fitted with experimental decay curves for determining the dipole-dipole interaction radius $R_{\text{d-d}}$, the saturation density n_0, and other parameters. However, since $R_{\text{d-d}}$ and n_0 are strongly correlated in these equations, a single decay curve is usually insufficient for determining both of them accurately. Instead, the fitting procedure must be performed simultaneously for a family of decay curves, which are measured by varying some experimental parameter, for example the number of photons in the pulse I_0. For this purpose, we have developed an advanced global nonlinear optimization package [34] based on a modified Levenberg-Marquardt algorithm [35]. For the fitting procedure we set $R_{\text{d-d}}$, n_0, and the decay time τ as global fitting parameters and the initial amplitude and background as local parameters for each curve. For a stable fitting procedure it is generally sufficient to fit the decay kinetics corresponding to about 10 different values of I_0.

2.3 Decay time temperature dependence of triplet excitons

While the mechanism of FRET leading to the nonlinear quenching of luminescence has been well understood in excitonic scintillators, a relation between the dipole-dipole interaction radius and the characteristics of the relaxed exciton, e.g., its localization, is unclear. Due to the complex crystal structure of tungstates and the fact that the exciton relaxation is accompanied by significant lattice distortions, a direct *ab initio* calculation for the estimation of exciton localization would be very challenging.

In this work, we shall indirectly try to establish a correlation between exciton localization and $R_{\text{d-d}}$ in tungstates by measuring the temperature dependencies of the intensity and the decay time of the intrinsic emission of $CaWO_4$, $SrWO_4$, and $BaWO_4$. Temperature dependence of the intensity is indicative of exciton diffusion, which is related to exciton localization. Temperature dependence of the decay time, if fitted to the model presented in this section, yields information about the spread of the electron component of the exciton, which is again related to exciton localization. Because the named crystals have a similar crystal (Table 2.1) and electronic structure and share the same luminescence mechanism, the results obtained from the temperature dependencies are expected to be directly comparable and will allow us to estimate the relative change of exciton localization in the series $CaWO_4 \rightarrow SrWO_4 \rightarrow BaWO_4$. By also determining the variation of $R_{\text{d-d}}$ in the given series, we can establish a relation between exciton localization and $R_{\text{d-d}}$.

The intrinsic emission of tungstates is generally attributed to the radiative recombination of STEs localized at the WO_4^{2-} molecular ions [37, 26, 38]. The exciton ground state has a triplet nature, with the lower lying energy level separated from the higher lying doubly degenerate level by an energy Δ_{SOC}, which is attributed to spin-orbit interaction (SOC). We shall model the temperature dependence of their decay time with a three level model that is based on [39].

The relaxed excitons populate the higher lying doubly degenerate level 2 and the lower lying metastable level 1 with the total population $n(t) = n_1(t) + 2n_2(t)$.

Table 2.1: Experimental and calculated lattice constants and the W-O bond lengths. The slight variation in the lattice parameters reflects the increase of the cation radius in the sequence Ca → Sr → Ba. See text (Sec. 4.3) for computational details.

		a (Å)	c (Å)	V (Å^3)	W-O (Å)
$CaWO_4$	exp[23]	5.2429	11.3737	156.32	1.782
	calc[a]	5.2290	11.2546	153.86	1.800
$SrWO_4$	exp[36]	5.4168	11.951	175.33	1.779
	calc[a]	5.4126	11.837	173.39	1.797
$BaWO_4$	exp[36]	5.6134	12.720	200.41	1.782
	calc[a]	5.6280	12.605	199.64	1.795

[a] Present work

This results in the coupled rate equations

$$\begin{aligned}\frac{\mathrm{d}n_1}{\mathrm{d}t} =& -k_1 n_1 - 2k_{12} n_1 + 2k_{21} n_2,\\ \frac{\mathrm{d}n_2}{\mathrm{d}t} =& k_{12} n_1 - k_2 n_2 - k_{21} n_2,\end{aligned} \tag{2.17}$$

where $k_{1,2}$ are the radiative transition rates from the levels 1,2 to the ground state and k_{12} and k_{21} are the nonradiative transition rates between levels 1 and 2. In the single-phonon approximation,

$$\begin{aligned}k_{21} =& K[1/(e^{\Delta_{\mathrm{SOC}}/k_B T} - 1) + 1],\\ k_{12} =& k_{21} e^{-\Delta_{\mathrm{SOC}}/k_B T} = K/(e^{\Delta_{\mathrm{SOC}}/k_B T} - 1),\end{aligned} \tag{2.18}$$

where K is the transition rate at $T = 0$. With analytical solutions of the form $n_i = A_i e^{-\lambda_i t}$ for $i = 1,2$, Eqs. (2.17) yield

$$\begin{aligned}2\lambda_\pm =& k_1 + k_2 + \chi_+ \pm \sqrt{(k_1 - k_2)^2 + \chi_+^2 + 2\chi_-(k_2 - k_1)},\\ \chi_\pm =& K\frac{e^{\Delta_{\mathrm{SOC}}/k_B T} \pm 2}{e^{\Delta_{\mathrm{SOC}}/k_B T} - 1}.\end{aligned} \tag{2.19}$$

$\tau_- = 1/\lambda_-$ and $\tau_+ = 1/\lambda_+$ are the equilibrium and the nonequilibrium decay times, respectively. In our experiments, only the equilibrium component was present in the decay of the intrinsic emission of the crystals. If we additionally account for the nonradiative quenching to the ground state [40], the observed decay time becomes

$$1/\tau_- = \lambda_- + K_x e^{-E_x/k_B T}, \tag{2.20}$$

where K_x is the quenching rate and E_x is the energy barrier. Such a substitution in Eq. (2.20) is justified if the high temperature plateau is reached at a lower temperature than the onset of thermal quenching.

Equation (2.20) can be fitted with experimental data to determine the transition rates $k_{1,2,12}$, the quenching parameters, and, most importantly, the spin-orbit splitting energy, Δ_{SOC}, between levels 1 and 2. Of all the atoms present in our systems, W has the biggest contribution to SOC because the splitting energy is proportional to Z^4, where Z is the nuclear charge. A variation in Δ_{SOC} of the crystals can be related to a variation in the time the electron spends in the vicinity of W. A smaller value of Δ_{SOC} can thus be translated into a larger spread of the exciton wavefunction.

2.4 Scintillator nonproportionality

A high energy resolution for the detection of high-energy particles is one of the most difficult constraints imposed on new scintillators. The energy resolution is defined as the full width at half maximum of the absorption peak in the pulse height spectrum divided by the energy of the exciting particle, $R = \Delta E/E$. It is mainly limited by the Poisson statistics of the emitted photons, intrinsic nonproportionality of the scintillator, and nonuniformities in the material. The latter is caused by the inhomogeneous distribution of activators (only in activated scintillators), various types of defects, and inhomogeneous distribution of unintentional impurities. Additional contribution to the energy resolution is from the photomultiplier tube (PMT) coupled to the scintillator. As scintillator crystals can now be grown with high purity and the PMT performance is already close to optimal, the only way to improve the energy resolution is to reduce the nonproportionality, and for this a better understanding of its causes is necessary.

Nonproportionality means that the total light output of the scintillator is not proportional to the energy of the absorbed high-energy particle. In other words, the scintillator yield, defined as the light output per energy deposited in the crystal (typically expressed in units of photons/MeV) is found not to be constant but vary with energy of the incident particle. For a proportional scintillator, the scintillator yield would be constant for all energies and the energy resolution would be limited only by Poisson statistics. For example, it has been determined that because of nonproportionality the energy resolutions of $\mathrm{LaBr_3}$:Ce, NaI:Tl, and LSO:Ce are 2.8 % (at 662 keV), 7 % (at 511 keV), and 9 % (at 511 keV), respectively, instead of the ideal values of 2.3 %, 3.8 %, and 4.2 % [41, 42].

In order to model scintillator nonproportionality for intrinsic excitonic scintillators such as those studied in this work, we shall assume the existence of linear radiative and nonradiative channels and a bimolecular nonradiative channel for the recombination of excitons. All the linear channels are indistinguishable in the rate equation and are covered by the single term proportional to $1/\tau$. Diffusion is assumed negligible. The scintillator yield can be expressed as

$$Y(E_0) = E_0^{-1} \int I_{\mathrm{lum}}(t, E_0)\,\mathrm{d}t, \tag{2.21}$$

where E_0 is the initial energy of the primary electron created by ionizing radiation and $I_{\text{lum}}(t, E_0)$ is the luminescence intensity along the track of the primary electron, explicitly dependent on the energy E_0. The luminescence intensity is given by

$$I_{\text{lum}}(E_0,t) = \frac{2\pi}{\tau}\int_0^{\infty} \rho\, \mathrm{d}\rho \int_0^{L(E_0)} \mathrm{d}x \frac{n(\rho,x)e^{-t/\tau}}{1+\frac{2}{3}\pi^2 n(\rho,x) R_{\text{d-d}}^3 \operatorname{erf}\left(\sqrt{t/\tau}\right)}, \tag{2.22}$$

which is identical to Eq. (2.10) except for the track length L instead of sample thickness z_0. The track length implicitly depends on E_0. The density of excitons n is proportional to the deposited energy E at a distance x. If we assume the track of the primary electron to have axial symmetry locally and assume a Gaussian distribution of secondary electronic excitations in the transversal direction then

$$n(\rho,x) = -\frac{\chi e^{-\rho^2/r_{tr}^2}}{\pi r_{tr}^2 E_{eh}} \left.\frac{\mathrm{d}E}{\mathrm{d}x'}\right|_{x'=x}, \tag{2.23}$$

where χ is the fraction of e-h pairs recombining into excitons, r_{tr} is the track radius, E_{eh} is the mean energy for the production of an e-h pair, and $\mathrm{d}E/\mathrm{d}x$ is the retarding force acting on the primary electron due to interaction with the crystal, also called the stopping power. E_{eh} is often taken as 2.5 times the (single-particle) band gap energy, $E_{eh} = 2.5E_g$. Accurate band gap energies can be obtained with the G_0W_0 method as described in the next section.

After the insertion of Eq. (2.23) into Eq. (2.22) the scintillator yield becomes

$$\begin{aligned} Y(E_0) &= \frac{1}{E_0}\int_0^{\infty} \mathrm{d}\xi \int_0^{E_0} \mathrm{d}E \frac{\chi e^{-\xi}}{E_{eh}} \frac{\ln[a(t)b(E)+1]}{a(t)b(E)}, \\ a(\xi) &= \frac{2\pi\chi R_{\text{d-d}}^3}{3 r_{tr}^2 E_{eh}} \operatorname{erf}\sqrt{\xi}, \\ b(E) &= -\left.\frac{\mathrm{d}E'}{\mathrm{d}x}\right|_{E'=E}. \end{aligned} \tag{2.24}$$

While there are many ways to approximate the stopping power $b(E)$, it is always a decreasing function of energy. The slower the primary electron travels through the crystal, the more energy it deposits. More energy is thus deposited at the end of the track, where the nonlinear luminescence losses are also greater. It follows that the greater the energy of the incident particle, the smaller is the overall relative loss of luminescence. In the limit of infinite E_0, $b(E)$ is always small except at the end of the track. There is thus negligible contribution from dipole-dipole interaction and the crystal becomes proportional in the high-energy limit. The proportionality is reflected in the constancy of the scintillator yield, which can be checked with the limiting case

$$\lim_{E_0\to\infty} Y(E_0) = \frac{\chi}{E_{eh}}. \tag{2.25}$$

Equation (2.25) follows from Eq. (2.24) based on the arguments presented above, but can also be tested using the explicit forms of $b(E)$ as given below. We can test another limiting case by switching off the dipole-dipole interaction, in which case Eq. (2.24) reduces to

$$\lim_{R_{\text{d-d}}\to 0} Y(E_0) = \frac{\chi}{E_{eh}} \tag{2.26}$$

and the crystal again becomes proportional. This result is expected since in our model the dipole-dipole interaction was assumed to be the only source of nonproportionality.

Stopping power. In the relativistic Born approximation, the stopping power is [11]

$$\begin{aligned} -\frac{\mathrm{d}E}{\mathrm{d}x} = &\frac{1}{\pi a_B E}\frac{2(1+E/mc^2)^2}{2+E/mc^2}\int_0^E \hbar\omega\,\mathrm{d}(\hbar\omega)\mathrm{Im}\left(-\frac{1}{\varepsilon(\omega,0)}\right) \\ &\times \ln\frac{\sqrt{E}\sqrt{E+2mc^2}+\sqrt{E-\hbar\omega}\sqrt{E+2mc^2-\hbar\omega}}{\sqrt{E}\sqrt{E+2mc^2}-\sqrt{E-\hbar\omega}\sqrt{E+2mc^2-\hbar\omega}}. \end{aligned} \tag{2.27}$$

In Eq. (2.27), the dependence of the imaginary inverse dielectric function (energy loss function) on momentum transfer has been neglected, i.e., $\mathrm{Im}\varepsilon^{-1}(\omega,\boldsymbol{q}) \approx \mathrm{Im}\varepsilon^{-1}(\omega,0)$, which follows from the assumption of mainly small-angle scattering [11]. Using the ionization potential approximation and considering the sum rules for the energy loss function, Eq. (2.27) reduces to

$$\begin{aligned} -\frac{\mathrm{d}E}{\mathrm{d}x} = &\frac{e^4}{4\pi\varepsilon_0 E}\frac{(1+E/mc^2)^2}{2+E/mc^2} \\ &\times \sum_i \frac{N_i}{V}\theta(E-I_i)\ln\frac{\sqrt{E}\sqrt{E+2mc^2}+\sqrt{E-I_i}\sqrt{E+2mc^2-I_i}}{\sqrt{E}\sqrt{E+2mc^2}-\sqrt{E-I_i}\sqrt{E+2mc^2-I_i}}, \end{aligned} \tag{2.28}$$

where I_i is the ionization potential of the ith core energy level, N_i is the number of electrons in the core level, and V is the unit cell volume. As an example, in $\mathrm{CdWO_4}$, if degeneracy is taken into account then, out of the total of 308 occupied states in the unit cell, there are 37 distinct ionization potentials that must be accounted for. Inserting Eq. (2.28) into Eq. (2.24) results in a fitting function that can be used on experimental nonproportionality data for determining the track radius r_{tr}, provided that the other parameters required by Eq. (2.24) are known. This includes $R_{\text{d-d}}$, which can be obtained from, e.g., photoexcitation experiments based on the theory of Sec 2.2.

In the nonrelativistic regime, Eq. (2.28) reduces to

$$-\frac{\mathrm{d}E}{\mathrm{d}x} = \frac{e^4}{8\pi\varepsilon_0 E}\sum_i \frac{N_i}{V}\theta(E-I_i)\ln\frac{\sqrt{E}+\sqrt{E-I_i}}{\sqrt{E}-\sqrt{E-I_i}}. \tag{2.29}$$

For energies larger than the ionization potentials, $E \gg I_i$,

$$-\frac{\mathrm{d}E}{\mathrm{d}x} = \frac{e^4}{8\pi\varepsilon_0 E}\sum_i \frac{N_i}{V}\ln\frac{4E}{I_i} = \frac{e^4}{8\pi\varepsilon_0 E}\frac{N}{V}\ln\frac{4E}{I}, \tag{2.30}$$

where the average ionization potential is defined according to $N\ln I = \sum_i N_i \times \ln I_i$. Equation (2.30) is also known as the nonrelativistic Bethe formula for the stopping power [43]. If Eq. (2.30) is inserted into Eq. (2.24) for the scintillator yield then, with the physically reasonable assumption that the electron can only lose and not gain energy, the lower bound of integration over energy should be modified from 0 to $I/4$. In this work, we shall test both (2.28) and (2.30) against experimental data in order to find the track radius and to estimate the accuracy of using the average ionization potential approximation and the nonrelativistic regime.

2.5 Electron-electron scattering

Secondary electrons and holes, which we call the particle track, are created as a result of inelastic scattering by the primary electron. The track formation takes place in the femtosecond time scale. This is followed by the thermalization stage, generally on the order of picoseconds, during which the particles diffuse with band velocities resulting in a finite track radius. For the well-known scintillators CaF_2, BaF_2, NaI, and CsI, the thermalization stage extends to approximately 0.5, 1, 2, and 7 ps [44]. In $CdWO_4$, thermalization has been estimated to be ≤ 0.5 ps [12].

The main scattering mechanism that limits electron and hole mobilities in a pure crystal is the electron-phonon interaction. The biggest contribution is from the absorption and emission of longitudinal optical phonons, and once the electron energy with respect to the conduction band minimum has fallen below that of optical phonons, interaction with acoustic phonons takes over [21]. There is, however, also some contribution from electron-electron scattering, which can in principle affect the mobilities. This is generally small and is not considered; to date, no studies have been performed to estimate the magnitude of electron-electron scattering during thermalization in scintillators. It is one of the purposes of this work to explicitly calculate the rates of electron-electron scattering for $CdWO_4$, a representative of the tungstates. The result is only qualitative in that the rates can be compared with the rates of electron-phonon scattering for judging the correctness of neglecting electron-electron scattering, but no matrix elements are calculated that could be used in the modeling of thermalization.

Quasiparticle lifetimes. Electron-electron scattering comes from the fact that the independent particle picture is not entirely valid in a real system. The electron and hole energy levels as calculated within the band theory are generally close to, but not the exact eigenstates of the many-body system. Because of this, the particles are scattering in and out of the single-particle levels, which are strictly speaking not stationary. The scattering rate is determined by the imaginary part of their complex eigenvalues.

Before proceeding, we remind that the true electron-electron scattering rate is probably quite high due to the strong Coulomb interaction, which certainly invalidates the single-particle picture. The latter survives, however, in terms of quasielectrons and -holes as envisaged in Landau's Fermi liquid theory [45]. The interaction between quasielectrons, which can be thought of as an electron plus its surrounding polarization cloud, is sufficiently weak for the single-particle picture to be approximately valid, and likewise for quasiholes. By electron-electron scattering we actually refer to the quasiparticle-quasiparticle scattering, whose calculation is one of the objectives of this work.

Mathematically, quasiparticles (QPs) are introduced by using the (relatively weak) dynamically screened potential

$$W(\boldsymbol{r},\boldsymbol{r}',\omega) = \frac{e^2}{4\pi\varepsilon_0}\int \frac{\varepsilon^{-1}(\boldsymbol{r},\boldsymbol{r}'',\omega)}{|\boldsymbol{r}''-\boldsymbol{r}'|}\,\mathrm{d}\boldsymbol{r}'' \tag{2.31}$$

instead of the bare Coulomb potential. In the QP approximation, the many-body excitation energies are determined by the QP equation,

$$(T+V_H+V_{\text{ext}})\psi_i^{\text{QP}}(\boldsymbol{r}) + \int \Sigma(\boldsymbol{r},\boldsymbol{r}',\varepsilon_i^{\text{QP}})\,\psi_i^{\text{QP}}(\boldsymbol{r}')\,\mathrm{d}\boldsymbol{r}' = \varepsilon_i^{\text{QP}}\psi_i^{\text{QP}}(\boldsymbol{r}), \tag{2.32}$$

where T, V_H and V_{ext} are the kinetic energy, the Hartree potential, and the external potential. The self-energy operator, written symbolically as $\Sigma = i\Gamma GW$ in terms of the vertex function, the Green's function, and the dynamically screened potential, represents the contribution from all the many-body effects that influence the particle's energy or its effective mass. In the context of condensed matter, it represents the potential felt by the electron due to all interactions with its immediate vicinity, which lead to the formation of a polarization cloud surrounding the electron, an effect that is energy dependent (hence the term *dynamical screening*). Standard techniques for solving Eq. (2.32) involve many-body perturbation theory (MBPT). The starting eigenfunctions and eigenvalues are usually obtained (nonperturbatively) from density functional theory (DFT) by solving the Kohn-Sham equations,

$$(T+V_H+V_{\text{ext}}+V_{xc})\psi_i^{\text{KS}}(\boldsymbol{r}) = \varepsilon_i^{\text{KS}}\psi_i^{\text{KS}}(\boldsymbol{r}), \tag{2.33}$$

where V_{xc} is the exchange-correlation potential and ψ_i^{KS} and $\varepsilon_i^{\text{KS}}$ are the Kohn-Sham wavefunctions and energies. The exchange-correlation potential can be thought of as a local, energy independent approximation to the self-energy. To first order, the QP energies are then given by

$$\varepsilon_i^{\text{QP}} = \varepsilon_i^{\text{KS}} + \left\langle \psi_i^{\text{KS}} \middle| \Sigma(\varepsilon_i^{\text{QP}}) - V_{\text{xc}} \middle| \psi_i^{\text{KS}} \right\rangle. \tag{2.34}$$

The difficulty with Eq. (2.34) is that Σ must be evaluated at the QP energy that we are trying to compute. However, because the self-energy is close to linear in energy [46], its value at $\varepsilon_i^{\mathrm{QP}}$ can be well approximated by

$$\Sigma(\varepsilon_i^{\mathrm{QP}}) \approx \Sigma(\varepsilon_i^{\mathrm{KS}}) + (\varepsilon_i^{\mathrm{QP}} - \varepsilon_i^{\mathrm{KS}}) \left. \frac{\partial \Sigma(\varepsilon)}{\partial \varepsilon} \right|_{\varepsilon = \varepsilon_i^{\mathrm{KS}}}, \tag{2.35}$$

in which case

$$\varepsilon_i^{\mathrm{QP}} = \varepsilon_i^{\mathrm{KS}} + Z^{-1} \left\langle \psi_i^{\mathrm{KS}} \middle| \Sigma(\varepsilon_i^{\mathrm{KS}}) - V_{\mathrm{xc}} \middle| \psi_i^{\mathrm{KS}} \right\rangle, \tag{2.36}$$

where

$$Z = 1 - \mathrm{Re} \langle \psi_i^{\mathrm{KS}} | \left. \frac{\partial \Sigma(\varepsilon)}{\partial \varepsilon} \right|_{\varepsilon = \varepsilon_i^{\mathrm{KS}}} | \psi_i^{\mathrm{KS}} \rangle \tag{2.37}$$

is the quasiparticle renormalization factor. Values of Z close to 1 imply well-defined single-particle-like excitations; typical values are around 0.8 [47]. The QP dispersion thus obtained is very close to the true band structure [48, 49, 50].

Once the QP eigenvalues have been calculated, the QP-QP (or electron-electron) scattering rate is given by [51]

$$\frac{1}{\tau_{n\boldsymbol{k}}^{\mathrm{QP}}} = \frac{2}{\hbar} \left| \mathrm{Im} \left\langle \psi_{n\boldsymbol{k}}^{\mathrm{KS}} \middle| \Sigma(\varepsilon_{n\boldsymbol{k}}^{\mathrm{QP}}) \middle| \psi_{n\boldsymbol{k}}^{\mathrm{KS}} \right\rangle \right|. \tag{2.38}$$

The use of the KS wavefunctions in Eq. (2.38) instead of the QP wavefunctions is well justified, since the two generally have about 99.9% overlap [52, 53]. The evaluation of Σ to a reasonable accuracy, however, can be a formidable task, especially for complex systems such as tungstates.

G$_0$W$_0$ approximation. The self-energy can in principle be accurately found as a self-consistent solution to Hedin's equations [54]. However, this would require calculating the Green's function to all orders of perturbation theory, which has about the same complexity as the many-body wavefunction and is not feasible in practice. A standard approach for approximating Σ is the so-called single-shot GW (G$_0$W$_0$) approximation, which refers to performing only the first iteration of Hedin's equations with the KS wavefunctions and energies as a starting point in the spirit of the "best G, best W" philosophy [47]. In the G$_0$W$_0$ approximation, the self-energy is

$$\Sigma(\boldsymbol{r}, \boldsymbol{r}', \varepsilon) = \frac{i}{2\pi} \int e^{i\varepsilon'\delta} G^{\mathrm{KS}}(\boldsymbol{r}, \boldsymbol{r}', \varepsilon + \varepsilon') W^{\mathrm{KS}}(\boldsymbol{r}, \boldsymbol{r}', \varepsilon')\, \mathrm{d}\varepsilon', \tag{2.39}$$

where G^{KS} and W^{KS} are the KS single-particle Green's function and the KS dynamically screened interaction and where $\delta \to 0^+$. In essence, the G$_0$W$_0$

approximation means keeping only the first term in the diagrammatic expansion of the electron's self-energy and neglecting any vertex corrections. If we return for a moment to the initial assumption of quasiparticles [Eq. (2.31)], it is worth noting that had we used the bare Coulomb interaction instead of W, the self-energy expansion would be severely divergent making the use of MBPT difficult or impossible [54].

Dividing the self-energy into exchange and correlation terms, $\Sigma = \Sigma^x + \Sigma^c$, the matrix elements are explicitly given as [55]

$$
\begin{aligned}
\langle \psi^{\mathrm{KS}}_{n\boldsymbol{k}} \,|\, \Sigma^x(\varepsilon^{\mathrm{KS}}_{n\boldsymbol{k}}) \,|\, \psi^{\mathrm{KS}}_{n\boldsymbol{k}} \rangle &= -\frac{e^2}{\varepsilon_0 V} \sum_m^{\mathrm{occ}} \sum_{\boldsymbol{G}\boldsymbol{q}} \frac{|M^{mn}_{\boldsymbol{G}}(\boldsymbol{k},\boldsymbol{q})|^2}{|\boldsymbol{q}+\boldsymbol{G}|^2}, \\
\langle \psi^{\mathrm{KS}}_{n\boldsymbol{k}} \,|\, \Sigma^c(\varepsilon^{\mathrm{KS}}_{n\boldsymbol{k}}) \,|\, \psi^{\mathrm{KS}}_{n\boldsymbol{k}} \rangle &= \frac{\hbar e^2}{\varepsilon_0 V} \sum_{m\boldsymbol{G}\boldsymbol{G}'\boldsymbol{q}} \int \mathrm{d}\omega' \\
&\quad \times M^{mn*}_{\boldsymbol{G}}(\boldsymbol{k},\boldsymbol{q}) M^{mn}_{\boldsymbol{G}'}(\boldsymbol{k},\boldsymbol{q}) J_{\boldsymbol{G}\boldsymbol{G}'}(\boldsymbol{k},\boldsymbol{q},\omega), \\
J^m_{\boldsymbol{G}\boldsymbol{G}'}(\boldsymbol{k},\boldsymbol{q},\omega) &= \frac{i}{2\pi} \frac{W_{\boldsymbol{G}\boldsymbol{G}'}(\boldsymbol{q},\omega) - v_{\boldsymbol{G}}(\boldsymbol{q})}{\hbar\omega + \hbar\omega' - \varepsilon^{\mathrm{KS}}_{m\boldsymbol{k}-\boldsymbol{q}} + i\delta \,\mathrm{sgn}(\varepsilon^{\mathrm{KS}}_{m\boldsymbol{k}-\boldsymbol{q}} - \mu)}, \\
M^{mn}_{\boldsymbol{G}}(\boldsymbol{k},\boldsymbol{q}) &= \langle \psi^{\mathrm{KS}}_{m\boldsymbol{k}-\boldsymbol{q}} | e^{i(\boldsymbol{q}+\boldsymbol{G})\boldsymbol{r}} | \psi^{\mathrm{KS}}_{n\boldsymbol{k}} \rangle,
\end{aligned}
\tag{2.40}
$$

where $W_{\boldsymbol{G}\boldsymbol{G}'}(\boldsymbol{q},\omega)$ is the double Fourier transform of the screened potential and where $v_{\boldsymbol{G}}(\boldsymbol{q}) = e^2/(\varepsilon_0|\boldsymbol{G}+\boldsymbol{q}|^2)$. The frequency integral along the real axis is rather ragged due to the presence of multiple poles and would in principle require the evaluation of the large $W_{\boldsymbol{G}\boldsymbol{G}'}(\boldsymbol{q},\omega)$ matrices at many different frequencies.

Integration along the real axis can be avoided by using the contour deformation technique [55]. Adding and subtracting an integral over imaginary frequencies allows to transform the frequency integral into

$$
\begin{aligned}
J^m_{\boldsymbol{G}\boldsymbol{G}'}(\boldsymbol{k},\boldsymbol{q},\omega) = &-\frac{1}{\pi} \int_0^\infty \mathrm{d}\omega' \frac{[W_{\boldsymbol{G}\boldsymbol{G}'}(\boldsymbol{q},\omega) - v_{\boldsymbol{G}}(\boldsymbol{q})](\hbar\omega - \varepsilon^{\mathrm{KS}}_{m\boldsymbol{k}-\boldsymbol{q}})}{(\hbar\omega - \varepsilon^{\mathrm{KS}}_{m\boldsymbol{k}-\boldsymbol{q}})^2 + (\hbar\omega')^2} \\
&\pm v_{\boldsymbol{G}}(\boldsymbol{q})[W_{\boldsymbol{G}\boldsymbol{G}'}(\boldsymbol{q},\omega\hbar - \varepsilon^{\mathrm{KS}}_{m\boldsymbol{k}-\boldsymbol{q}}) - v_{\boldsymbol{G}}(\boldsymbol{q})] \\
&\times \theta[\pm(\varepsilon^{\mathrm{KS}}_{m\boldsymbol{k}-\boldsymbol{q}} - \mu)]\theta[\pm(\hbar\omega - \varepsilon^{\mathrm{KS}}_{m\boldsymbol{k}-\boldsymbol{q}})].
\end{aligned}
\tag{2.41}
$$

The contribution along the imaginary axis is fairly smooth and can be accurately determined using, e.g., Gaussian quadrature for only a few distinct ω. The second contribution from the poles is found by explicitly calculating $W - v$ for some frequencies and interpolating for the intermediate values. While this technique greatly simplifies the original integral, the evaluation of the matrix elements can still be quite expensive due to the necessity of calculating up to thousands of empty states for satisfactory convergence. The scaling with system size is about $O(N^4)$.

DFT band gap problem. Besides being able to give the quasiparticle lifetimes, the G_0W_0 method also yields accurate band gaps (within ~ 0.1 eV). In the present context, the band gap values are required for estimating the mean energies for the production of electron-hole pairs in our nonproportionality model (Sec. 2.4). To date, no direct direct measurements of the band gap have been performed for any of the tungstates.

The most popular method for calculating electronic structures is the relatively cheap density functional theory. However, standard DFT calculations typically underestimate band gap values by about 40% [56]. In principle, the band gap is accurately given by

$$\Delta = \varepsilon_{N+1}^{\mathrm{KS}}(N) - \varepsilon_{N}^{\mathrm{KS}}(N) + \left.\frac{\delta E_{xc}[n]}{\delta n(\boldsymbol{r})}\right|_{n=N+\delta} - \left.\frac{\delta E_{xc}[n]}{\delta n(\boldsymbol{r})}\right|_{n=N-\delta}, \tag{2.42}$$

where $\varepsilon_m(N)$ is the mth KS eigenvalue of an N-electron system and where the second part is the discontinuity in the functional derivative of the exchange-correlation energy with respect to the number of particles. The derivative discontinuity is always present in semiconductors and insulators and is the main reason for the underestimation of band gaps [56, 57]. None of the currently available approximations for the exchange-correlation energy are able to reproduce the discontinuity. Sometimes it is inserted manually based on experimental data, in which case it is called the scissor operator.

The origin of the band gap underestimation is related to the local, energy independent approximations for the exchange-correlation energy that are commonly used in DFT calculations. By contrast, the self-energy used in quasiparticle calculations is nonlocal and, most importantly, energy dependent, which allows to correctly account for electron correlation and leads to much more accurate excited state eigenvalues.

Chapter 3

EXPERIMENTAL

Crystals. In this work, we used the undoped crystals of $CdWO_4$, $CaWO_4$, $SrWO_4$, and two samples of $BaWO_4$ of different origin. The samples of $CaWO_4$, $SrWO_4$, and one of the samples of $BaWO_4$ were grown at the General Physics Institute, RAS, Russia. The other $BaWO_4$ sample was grown at the Institute for Solid State Physics and Optics, Wigner Research Centre for Physics, HAS, Hungary. $CdWO_4$ was grown at the Institute for Single Crystals, Kharkov. All samples were grown by the Czochralski method. The crystals were cleaved in the (010) plane and the excitation of the crystals was performed along the $\langle 010 \rangle$ axis.

Nonlinear decay kinetics. In order to experimentally observe FRET in the decay kinetics of the exciton luminescence in insulators, very high excitation densities must be used. This comes from the requirement that the average separation between the small-radius Frenkel excitons be sufficiently small for FRET to be efficient. Femtosecond laser systems provide a controllable environment for achieving such densities.

We have performed experiments at the Laser Research Center of Vilnius University and at the PLFA facility, CEA-Saclay, France for studying the nonlinear decay kinetics of exciton luminescence in tungstates.

The Ti:Sapphire fs-laser at Vilnius University uses Kerr-lens modelocking with a Superspitfire amplifier (Spectra Physics, USA). The TOPAS-800 amplifier (Light Conversion Ltd, Lithuania) and frequency mixers provide wavelength tuning in a wide range of 189 nm – 20 μm. In our experiments, the pulse duration was 100 fs and the maximum excitation power density $\sim 10^{12}$ W/cm^2. The beam radii were determined with a CCD camera. A half-wave plate and a polarizing mirror were used to control the pulse energy. Luminescence was analyzed with a Hamamatsu R2059 photomultiplier (2.6 ns resolution) and a digital 4 GS/s LeCroy oscilloscope. Decay curves were averaged over 10 000 excitation pulses and consisted of 9000 data points. Excellent beam stability ($< 3\%$) resulted in low noise and good reproducibility of the measured curves. For temperatures other than room temperature, a cryostat with quartz windows was used.

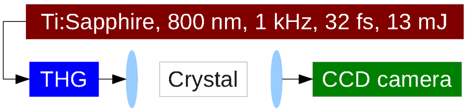

Figure 3.1: Experimental setup at CEA-Saclay. The first and second lenses have the focal lengths of 100 cm and 5 cm, respectively. Spot size on the crystal is 102 µm.

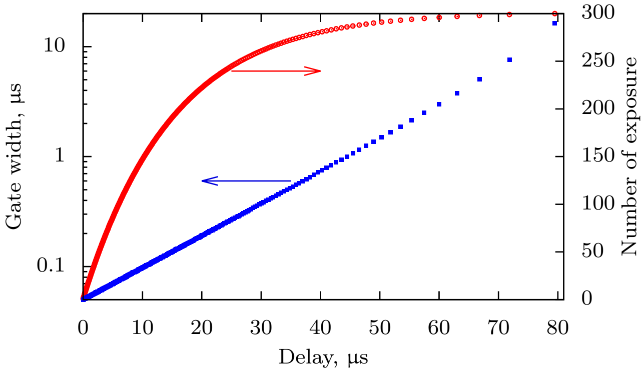

Figure 3.2: Gate width (squares) as a function of delay from the laser pulse and the corresponding number of exposure (circles).

The Ti:Sapphire laser at CEA-Saclay is based on chirped pulse amplification and is capable of producing 13 mJ pulses with a duration of 32 fs, repetition rate of 1 kHz and peak power of 0.4 TW. Generation of the second, third, and fourth harmonic is also possible. We used the third harmonic (THG) with the excitation wavelength of 266 nm, pulse energy up to 20 µJ and pulse duration of 80 fs. Luminescence was recorded with a gated CCD camera allowing for both spatially and temporally resolved measurements (Fig. 3.1). The Andor iStar intensified CCD camera has a 1024 × 1024 resolution which, in combination with magnification by a lens, covers an area of $520 \times 520\ \mu\text{m}^2$ on the crystal surface. Gate width was varied so that to be shorter initially and longer for larger time delays. This served the purpose of having both better temporal resolution at the beginning of the decay curves, where the nonlinear phenomena mainly take place, and keeping the accumulated signal intensity approximately constant in the camera. The gate width was varied from 50 ns at the beginning to longer than 10 µs at the end of an event (Fig. 3.2). The evolution of the luminescence image with a spatial resolution of 0.5 µm was recorded as a luminescence 'movie' of 300 exposures within an 80-µs time interval. In order to compensate a slight spot wobbling for subsequent pulses, the positions of the maxima of the signal intensity distributions were shifted to coincide for each image. The positions were determined by fitting with Gaussians in two directions. After the stabilization procedure, the decay curves corresponding to different points on the crystal surface could be extracted, providing a unique opportunity to study the exciton-exciton interaction across the beam profile. Additional information that could be extracted from the data was the spatial distribution of the luminescence yield, which results from the time integration of the images corresponding to a given event. The sum of pixel intensities over an image yields spatially integrated luminescence curves analogous to those usually recorded with a photomultiplier. The $1/e$ beam radius was determined from the first image taken at the lowest pulse energy of 20 nJ. The choice of the lowest pulse energy ensured minimal distortion of the Gaussian beam profile due to the nonlinear effects.

Low excitation density measurements. Before determining the temperature dependencies of the intensity and the decay time of the intrinsic emission, we first attempted to identify the intrinsic emission by measuring the time-resolved emission spectra of $CaWO_4$, $SrWO_4$, and $BaWO_4$. The spectra and the temperature dependencies were measured with 1 μs pulses using a xenon Perkin-Elmer FX-1152 Flashtube and an Ortec MCS-PCI Card with a 100 ns resolution. Emission and excitation wavelengths were selected with double-quartz monochromators DMR-4. The emission was detected with a Hamamatsu photon counting head H6240-01.

Chapter 4

RESULTS

4.1 Nonlinear decay kinetics of exciton luminescence

Luminescence decay curves. We have recorded the decay kinetics of the intrinsic emission of $CdWO_4$, $CaWO_4$, and $SrWO_4$ under high excitation density conditions [58, 16]. For $BaWO_4$, we could not identify the intrinsic emission (see Sec. 4.3). Figure 4.1 presents normalized decay curves of $CdWO_4$ at 301.9 nm (4.1 eV) excitation. Since the optical gap of $CdWO_4$ is 4.8 eV [28, 16], this falls in the low-energy part of the Urbach tail. In the low density regime, the decay would be purely exponential with a decay time of 15 µs at room temperature [59]. As the excitation density increases, the decay curves start showing nonexponentialities in the beginning. The nonexponentiality, which is due to the nonradiative energy transfer between excitons, becomes more pronounced with excitation density, as has been observed before [13, 14]. As a consequence, the relative losses of luminescence are seen to increase with pulse energy in Fig. 4.1.

In addition to the effects of exciton-exciton interaction, Fig. 4.1 also reveals the presence of the saturation effect. As the pulse energy is increased from 0.07 to 0.96 µJ, the decay becomes more nonexponential. However, for higher energies the shape of the curves remains practically unchanged. This is indicative of some saturation mechanism limiting the density of excitons and therefore the efficiency of nonradiative energy transfer between excitons at high laser pulse energies. Within the framework of the model of Sec. 2.1, this is explained by the existence of a limit to the exciton density, n_0, in the sample due to absorption saturation. The efficiency of nonradiative transitions responsible for the initial nonexponentiality is directly related to the exciton density. The closer the exciton density gets to n_0, the more transparent the crystal becomes locally and therefore very high energy pulses simply penetrate deeper into the crystal without changing the shape of the decay curve much. Further discussion on the saturation effect is deferred to Sec. 4.2.

The decay curves recorded for $CaWO_4$ and $SrWO_4$ (not shown) showed qualitatively the same features and are subject to the same conclusions. The

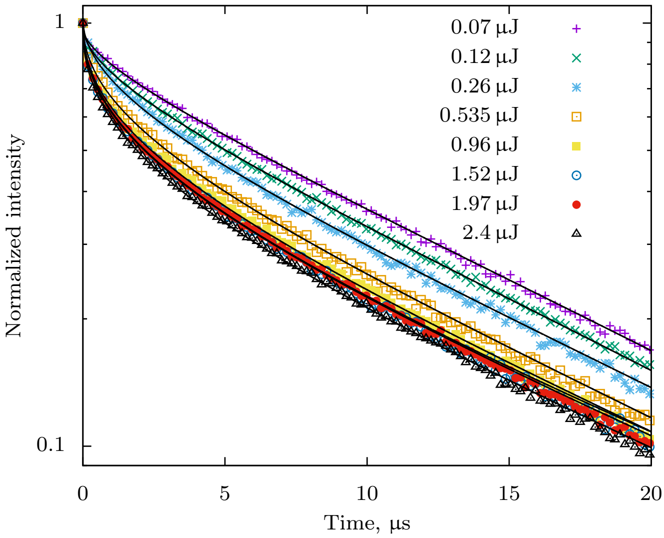

Figure 4.1: Decay curves of the intrinsic emission of $CdWO_4$ at 301.9 nm excitation for different pulse energies. Black lines are fits with Eq. (2.12). For better visualization the data is averaged over 40 data points.

thickness and the absorption coefficient of each crystal were sufficiently high so that $z_0\alpha \gg 1$ for all cases, allowing us to use Eq. (2.12) for the fitting procedure. The results of the fitting procedure are summarized in Table 4.1. The absorption coefficients were directly measured up to values on the order of 100 cm^{-1} and then extrapolated according to the Urbach law. In the wolframite-structured $CdWO_4$, the dipole-dipole interaction radius is 3.65 nm. We believe this to be more accurate compared to the previously reported values for $CdWO_4$ [13, 14] due to a better knowledge of the parameters necessary for the fitting procedure. In particular, the absorption coefficient and the exciton yield (number of excitons created by one photon) are accurately known in the Urbach tail, as opposed to the fundamental absorption region. From other known scintillators, $R_{\text{d-d}}$ has been determined to be 2.9 nm for CsI and 5.0 nm for the triplet emission of NaI [32].

In the scheelites of $CaWO_4$ and $SrWO_4$, $R_{\text{d-d}}$ is 3.2 nm and 5.8 nm, respectively. Because the probability of energy transfer between a pair of excitons is proportional to $R_{\text{d-d}}^6$, FRET seems to be much more efficient in $SrWO_4$ than in $CaWO_4$. Given the similar ground state crystal and electronic structures, such a drastic difference is puzzling. In Sec. 4.3, it will be attributed to the differences in the excited state structural relaxation of these crystals.

Spatially-resolved decay kinetics. At CEA-Saclay, the time-resolved luminescence images of $CdWO_4$ were recorded at an excitation wavelength of 266 nm

Table 4.1: Results of the fitting procedure with Eq. (2.12). 8, 9, and 10 curves were simultaneously fitted for $CdWO_4$, $CaWO_4$ and $SrWO_4$, respectively, with pulse energies ranging from 0.07 μJ to 2.4 μJ.

	$CdWO_4$	$CaWO_4$	$SrWO_4$
T	295 K	92 K	92 K
λ	301.9 nm	240.5 nm	240.5 nm
a	19.8 μm	71.8 μm	24.3 μm
α	$1036\,\mathrm{cm}^{-1}$	$7067\,\mathrm{cm}^{-1}$	$479\,\mathrm{cm}^{-1}$
z_0	1.26 mm	2 mm	> 1 mm
αz_0	130	1413	> 47.9
τ	14.1 μs	17.6 μs	29.9 μs
$R_{\text{d-d}}$	3.65 nm	3.17 nm	5.84 nm
n_0	$5.31 \times 10^{18}\,\mathrm{cm}^{-3}$	$2.90 \times 10^{18}\,\mathrm{cm}^{-3}$	$5.84 \times 10^{17}\,\mathrm{cm}^{-3}$

(4.66 eV) with pulse energies in the range of 20 nJ – 1 μJ. Figure 4.2 presents the distribution of light sum measured at 60 nJ and 300 nJ. The distribution is flatter for the higher energy, which indicates a greater efficiency of exciton quenching at higher excitation densities. The laser beam profile was the same for both cases.

The pulse radius of 102 μm was determined from the first image that was recorded at the pulse energy of 20 nJ (Fig. 4.3), displaying an almost perfect Gaussian intensity distribution. Figure 4.4 presents several decay curves recorded at different distances from the pulse center, which we define as the intersection of the crystal surface and the symmetry axis of the beam, which is the point of maximum excitation density. The curves correspond to square-shaped areas of $66\,\mu\mathrm{m}^2$ on the crystal surface. We see that a higher exciton density leads to a greater nonexponentiality at the beginning of the curves, which turn to almost single exponentials in the low-intensity regions of the image. The data presented in Figs. 4.2 and 4.4 are a unique attempt to visualize the effects of exciton-exciton interaction at the microscopic scale.

At 266 nm, data analysis is more complicated due to the unknown value of the absorption coefficient, which is too high to be measured directly or extrapolated with the Urbach law. However, it can be calculated from

$$\alpha(\omega) = \sqrt{2}\frac{\omega}{c}\sqrt{|\varepsilon(\omega)| - \mathrm{Re}\varepsilon(\omega)}, \tag{4.1}$$

where ε is the dielectric function. Figure 4.5 presents the absorption coefficient for two different polarization directions. For the fitting procedure, we set the value of the absorption coefficient to $3.17 \times 10^5\,\mathrm{cm}^{-1}$, which corresponds to the average of the two directions.

Since the excitation density can be considered nearly constant within an area of $66\,\mu\mathrm{m}^2$, Eq. (2.15) is the correct fitting function for this case. 7×7 curves with

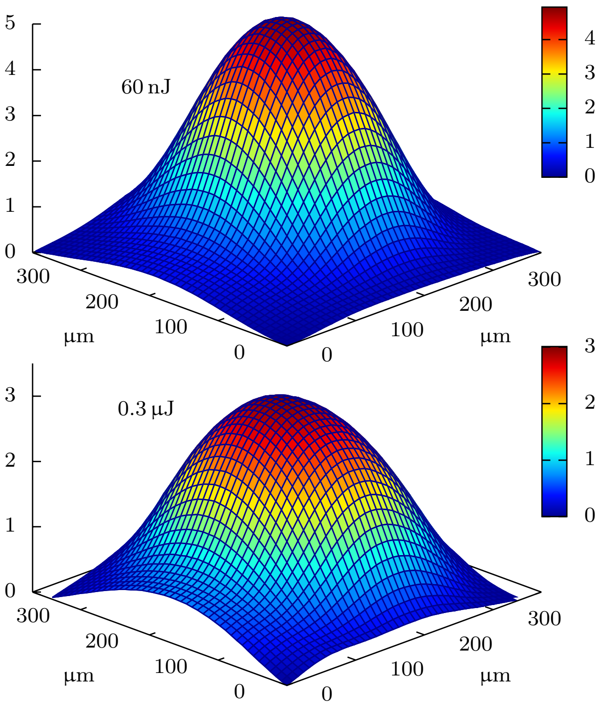

Figure 4.2: Spatial distribution of time-integrated luminescence intensity of $CdWO_4$ at two different pulse energies at 266 nm excitation. The images have been averaged over 16×16 data points.

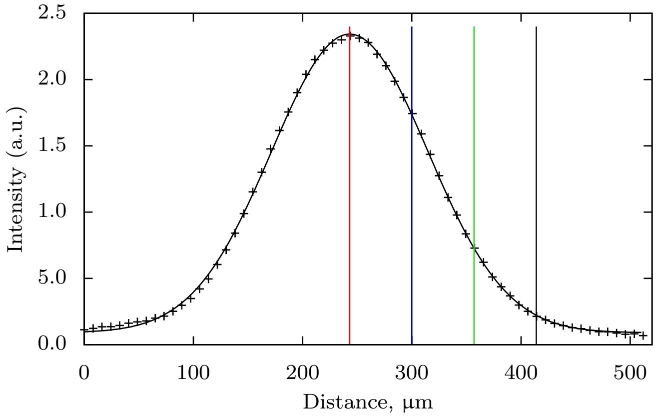

Figure 4.3: Luminescence intensity integrated over the first 50 ns and one spatial direction under excitation at 266 nm at 20 nJ pulse energy. The symbols are data points, the solid line is a fit by a Gaussian. Vertical lines mark the distances from the pulse center at which the decay kinetics is shown in Fig. 4.4.

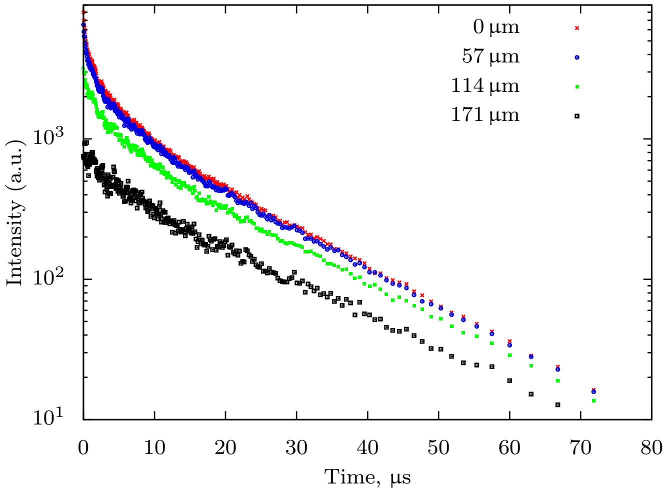

Figure 4.4: Decay curves at different distances from the pulse center measured at the pulse energy of 0.3 µJ. The curves represent the average luminescence intensity corresponding to 66 μm^2 square-shaped spots on the crystal and may be fitted to Eq. (2.15).

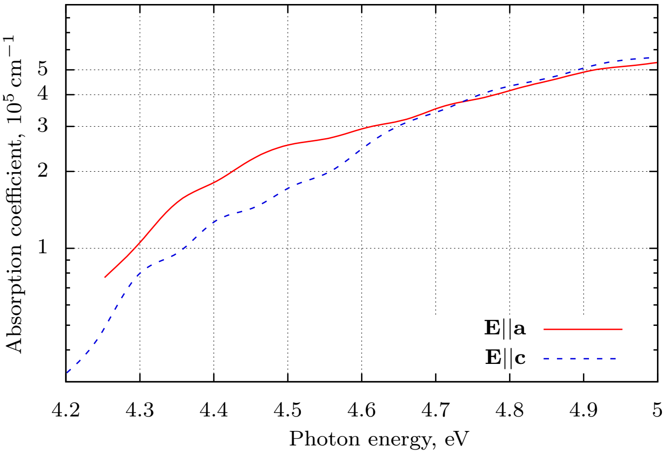

Figure 4.5: Absorption coefficient as calculated using Eq. (4.1) with the electric field of the incident light parallel to the *a*-axis (solid) and *c*-axis (dashed). The dielectric function for both cases is taken from [60].

equal spacing from a $171 \times 171\ \mu\mathrm{m}^2$ area were chosen to be fitted simultaneously (with a total of 101 fitting parameters). In Eq. (2.15), we set $I_0 \to I_0 \Delta S e^{-\rho^2/a^2}$, where $\Delta S = 66\ \mu\mathrm{m}^2$, $a = 102\ \mu\mathrm{m}$, and ρ is the distance from the pulse center. For the 1 μJ pulse energy, the fitting results were $R_{\text{d-d}} = 3.99\,\mathrm{nm}$, $\tau = 16.1\ \mu\mathrm{s}$, and $n_0 = 1.89 \times 10^{19}\,\mathrm{cm}^{-3}$. For 300 nJ the results were $R_{\text{d-d}} = 3.46\,\mathrm{nm}$, $\tau = 16.5\ \mu\mathrm{s}$, and $n_0 = 2.05 \times 10^{19}\,\mathrm{cm}^{-3}$. These kind of fluctuations in the value of $R_{\text{d-d}}$ were expected due to poor beam stability and the sensitivity of the fitting parameters. The fitting procedure failed to converge for lower pulse energies due to low signal. We accept that the best estimates are the averaged values of $n_0 \approx 1.9 \times 10^{19}\,\mathrm{cm}^{-3}$ and $R_{\text{d-d}} \approx 3.7\,\mathrm{nm}$ (including the value obtained at 301.9 nm excitation).

Under excitation by 80-fs pulses at 4.84 eV, $R_{\text{d-d}}$ has been estimated to be 3 nm [14]. Such excitation energy is near the energy of resonant exciton absorption, where Eq. (2.13) is assumed to be valid. In that study, the absorption coefficient was unknown and was taken from general considerations as $10^6\,\mathrm{cm}^{-1}$. Using the corrected value of $R_{\text{d-d}} = 3.7\,\mathrm{nm}$ and taking into account that $R^3_{\text{d-d}}$ and α are coupled in Eq. (2.13), we can correct the absorption coefficient at 4.84 eV to $(3/3.7)^3 10^6\,\mathrm{cm}^{-1} = 5.3 \times 10^5\,\mathrm{cm}^{-1}$. This is close to the value $\alpha = 4.7 \times 10^5\,\mathrm{cm}^{-1}$, which can be obtained by averaging the absorption coefficients at 4.84 eV for two polarizations in Fig. 4.5. If all the necessary parameters are known with sufficient accuracy, the $R_{\text{d-d}}$ value determined at some energy could in principle be used to determine the absorption coefficient at any other energy, including regions where it would normally be too high to be measured directly.

4.2 Absorption saturation

That the saturation effect is present in our experiments is supported by the fact that the saturation model fits the decay curves perfectly (Fig. 4.1), in addition to the qualitative features of the decay curves as discussed in Sec. 4.1. We have also tried to fit the decay curves with Eq. (2.13), which is the $n_0 \to \infty$ limit of the present model [Eq. (2.12)] and which has been used in the previous studies. Because it only accounts for the dipole-dipole interaction and not absorption saturation, it was not possible to get a good fit. Similarly, it was not possible to fit the decay curves corresponding to small patches on the crystal surface, such as those displayed in Fig. 4.4, to Eq. (2.16), which is the $n_0 \to \infty$ limit of Eq. (2.15). It has to be noted that for individual curves one would get a good fit using either model. However, in order to have a good global fit, the fitting function needs to correctly reproduce the dependence of the shape of the decay curve on pulse energy. Because of the global constraints, the fitting curves corresponding to the older model are unable to correctly pass an entire family of experimental curves.

The saturation density n_0 depends on the pulse duration and the exciting photon energy. For lower excitation energies, n_0 is smaller due to the smaller

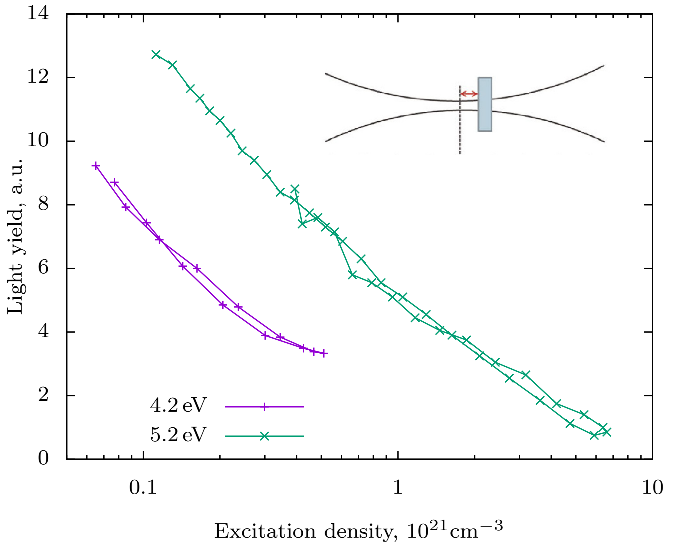

Figure 4.6: Light yield dependence on the maximum exciton density at 4.2 eV and 5.2 eV excitation. Inset is a schematic of the Z-scan method used to obtain the dependencies. The reason we see two approximately overlapping dependencies for either energy is that as the crystal moves past the focus, the excitation density starts decreasing again.

number of centers possessing the atomic configuration favorable for excitation, and correspondingly the saturation effect will manifest itself at lower excitation densities. In Sec. 4.1, we have shown this to be true for $CdWO_4$, where the n_0 values were 5.31×10^{18} and 1.9×10^{19} cm^{-3} at 4.1 and 4.66 eV, respectively. The fact that we were unable to get a good fit at 4.66 eV with the older model, which is close to the optical gap of 4.8 eV, is unsurprising considering that even close to the band gap lattice vibrations still play the dominant role in absorption [61].

Figure 4.6 presents the light yield dependence on the exciton density at the pulse center for two photon energies — one from the Urbach tail and one from the fundamental absorption region. The data is obtained from Z-scan measurements, where the exciton density is calculated as

$$\begin{aligned} n^{\max}(z) =& \frac{N_0 \alpha}{\pi a^2(z)}, \\ a(z) =& a_0 \sqrt{1 + \left(\frac{M^2 \lambda z}{2\pi a_0^2}\right)^2}, \end{aligned} \tag{4.2}$$

where a_0 is the $1/e$ beam radius, M^2 is the laser beam quality factor, λ is the photon wavelength, N_0 is the number of photons in the pulse, and z is sample distance from the beam focus. The light yield can be thought of as a measure of the

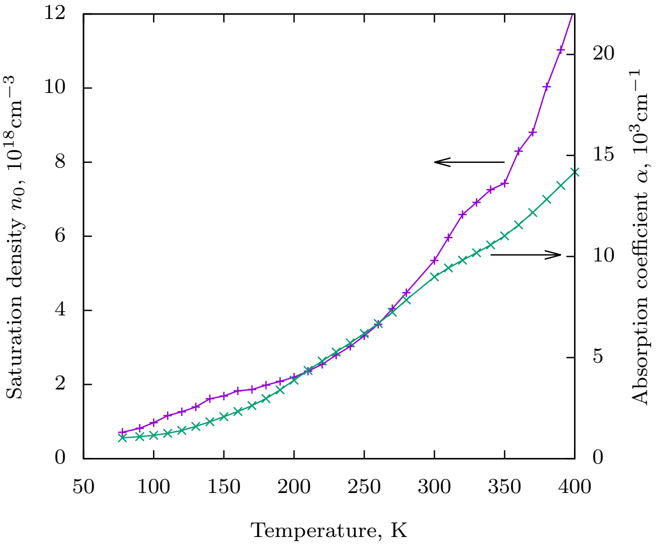

Figure 4.7: Temperature dependence of the saturation density and the absorption coefficient of $CdWO_4$ at the excitation energy of 4.2 eV (optical gap ~4.8 eV). Each data point was determined by fitting the measured luminescence decay curve to Eq. (2.12). $R_{\text{d-d}}$ value was fixed at 3.7 nm.

average exciton density in the crystal — the higher the density, the lower the light yield due to the nonlinear losses of luminescence. If the only nonlinear effect were from the dipole-dipole interaction, then the exciton density could grow without limit (strictly speaking until $1/V$, where V is the unit cell volume). However, at 4.2 eV the decreasing of the light yield slows down at a lower exciton density than at 5.2 eV. This can be attributed to the saturation effect that is present only at 4.2 eV and is inhibiting a further increase of the exciton density.

In addition to the energy dependence, the saturation effect should also have a temperature dependence. Even though the phonon picture is not applicable in the femtosecond time frame, the number of centers capable of absorption at the moment of excitation, n_0, is still expected to be correlated with the phonon distribution of the crystal. It follows that, for a fixed energy, n_0 should increase monotonically with increasing temperature just as the phonon population does. Such behavior is indeed present in Fig. 4.7, where, in the temperature range of 78–400 K, n_0 increases from the order of $10^{18}\,\mathrm{cm}^{-3}$ to the order of $10^{19}\,\mathrm{cm}^{-3}$. In addition, since both n_0 and the linear absorption coefficient α are proportional to the total number of levels $n_1 + n_2$ in the two-level model, they are expected to follow the same temperature dependence. This holds approximately true until room temperature (Fig. 4.7), after which the model is probably not applicable due to the thermal quenching of excitons in $CdWO_4$ [62].

Since both α and n_0 are proportional to $n_1 + n_2$, they are also proportional to each other. α additionally depends on the dipole matrix elements between the valence and conduction states. If we take the matrix elements to be the same for $CaWO_4$ and $SrWO_4$ because of the similar electronic structure, then their n_0 values become directly comparable. It follows that since in our experiments $SrWO_4$ had a lower α it should also exhibit a lower n_0. Such conclusion in indeed confirmed by the results of Table 4.1.

4.3 Correlation between the exciton radius and the dipole-dipole interaction radius

Time-resolved emission spectra. In order to explain the large difference in the $R_{\text{d-d}}$ values of $CaWO_4$ and $SrWO_4$, we attempted to find any noticeable differences in the relaxed exciton characteristics from low excitation density experiments.

Figure 4.8 presents the time-resolved emission spectra and the excitation spectra of $CaWO_4$, $SrWO_4$, and two samples of $BaWO_4$ of different origin, all measured at 4.2 K. The emission spectra were obtained by measuring the decay kinetics at each emission energy and fitting the resulting decay curves to a sum of at most four exponentials and background. Each data point in the figure corresponds to the light sum $I_{0n}\tau_n$, where I_{0n} and τ_n are the initial amplitude and the decay time of the nth decay component. Relative values of the light sums corresponding to a given crystal and excitation energy are directly comparable.

Tungstates are characterized by an intrinsic blue emission, which typically peaks in the region 2.5–2.9 eV [26, 25, 59, 63], and a defect green emission, which peaks in the region 2.3–2.4 eV [25, 26, 37]. The blue band is related to the recombination of STEs localized at the WO_4^{2-} complexes and the green band to lattice defects, most frequently to WO_3 Schottky defects.

We measured the emission spectra for two excitation energies — one corresponding to the band gap edge and one exciting to the fundamental absorption region. Similarly, we attempted to measure the excitation spectra for the green and blue luminescence, although for $BaWO_4$, as explained below, the latter was not identifiable.

Both $CaWO_4$ and $SrWO_4$ display an intrinsic emission band at around 2.8 eV and a defect emission band at 2.4 eV, which are the characteristic blue and green luminescence [64, 26, 65]. The corresponding luminescence decay times for $CaWO_4$ are 366 μs (a4 in Fig. 4.8) and 551 μs (a1). In addition to the main green band, there are two other bands (a2, a3) at 4.5 eV excitation, which are about 5 times weaker at the maximum. The blue band of $SrWO_4$ is resolved into 254 (b3) and 1.0 μs (b4) components, the latter being 100 times weaker. The green band consists of 522 μs (b1) and 40 μs (b2) components, the latter being about 10 times

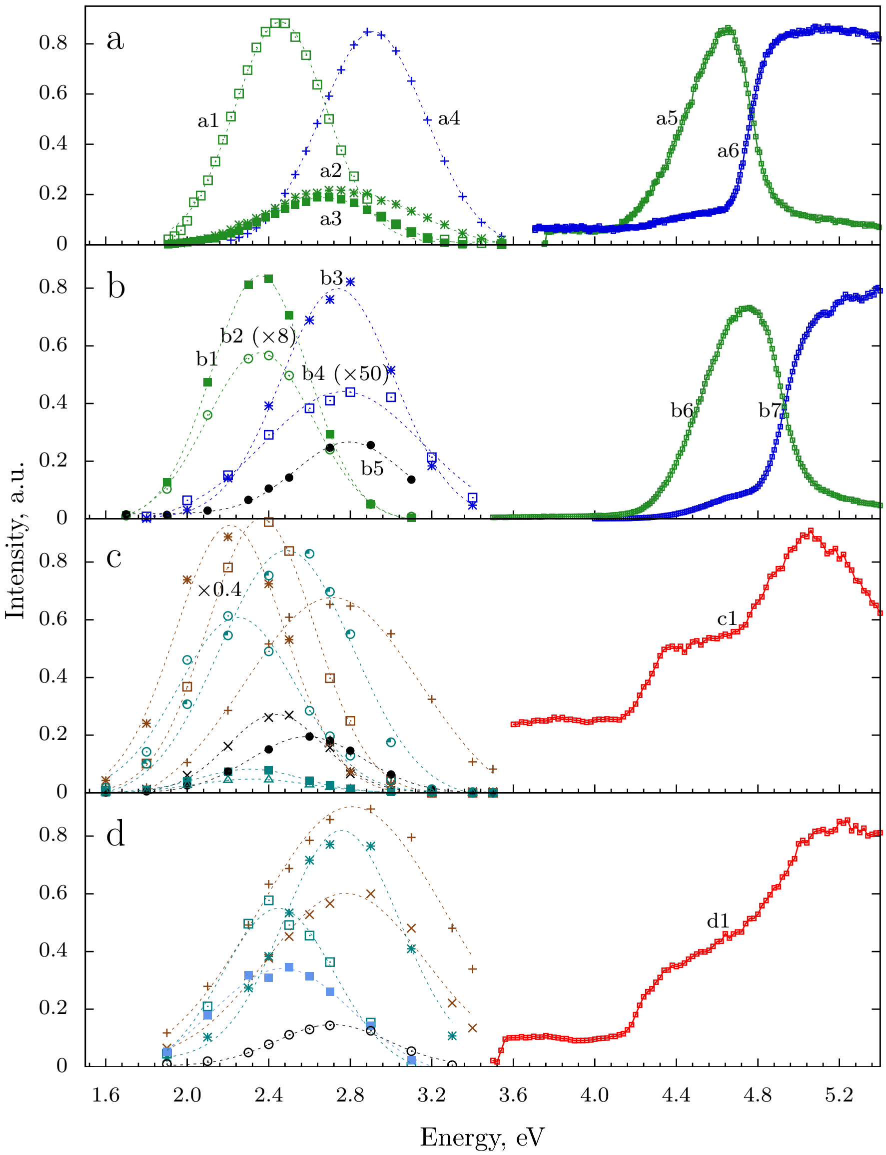

Figure 4.8: Emission and excitation spectra of CaWO$_4$ (a), SrWO$_4$ (b), and two BaWO$_4$ (c,d) crystals at 4.2 K. Emission energies used for excitation are 2.10 (a5), 2.76 (a6), 2.0 (b6), 2.85 (b7), 2.7 (c1), and 2.75 eV (c2). Excitation energies for measuring emission are 4.5 (a1, a2, a3), 5.2 (a4), 4.5 (b1, b2), and 5.2 eV (b3, b4, b5). The decay times and excitation energies for the emission of BaWO$_4$, in the order of decreasing maximum intensity, are c) 16 ms (3.7 eV), 1.8 ms (3.7 eV), 22 ms (4.45 eV), 7.7 μs (3.7 eV), 1.5 ms (4.45 eV), $>$ 10 ms (3.7 eV), $>$ 10 ms (4.45 eV), 26 μs (4.45 eV), 72 μs (4.45 eV) and d) 0.9 μs (3.75 eV), 15 μs (4.45 eV), 8.3 μs (3.75 eV), 151 μs (4.45 eV), 2.2 μs (5.2 eV), $>$ 10 ms (5.2 eV). Symbols are the light sums. Dotted lines are Gaussian fits.

weaker. There is an additional long component at 2.8 eV (b5), which manifests itself in the energy dependence of background and must have a decay time of at least 10 ms. The fundamental absorption region starts at a higher energy in $SrWO_4$ than in $CaWO_4$ in accordance with [66], where the band gaps of tungstates were predicted to grow with cation size.

For both $BaWO_4$ crystals we could distinguish about ten emission components at different excitation wavelengths, of which the most intense ones are shown in Fig. 4.8. The decay times ranged from less than 1 μs to more than 10^4 μs (see the caption of Fig. 4.8). Notably, there is no clear agreement in the position of the bands or the decay times between the two samples. There is also some disagreement in the excitation spectra of the two samples, whose complicated structure, possibly a result of several defect centers, is in contrast to $CaWO_4$ and $SrWO_4$, where the green and blue components are clearly identified. Previously, weak intrinsic emission of $BaWO_4$ has been claimed to be seen at approximately 2.7 eV [67, 63]. However, with no time-resolved analysis such assignment can be dubious, since our stationary emission spectra of $BaWO_4$ (not shown) also resemble single Gaussians and seemingly agree with those of [67, 63]. We can conclude that the emission bands of the $BaWO_4$ samples originate mainly from defect centers, which are expected to be sample dependent. The intrinsic luminescence is either too weak to be distinguished from defect luminescence or it is nonexistent in $BaWO_4$.

Decay time temperature dependence. Having distinguished the characteristics of the decay kinetics of the intrinsic and extrinsic emission of $CaWO_4$ and $SrWO_4$, we further investigated the nature of the exciton states responsible for the intrinsic emission by measuring the temperature dependence of their decay time. In $BaWO_4$, no decay components identifiable as intrinsic emission could be separated. Neither had the decay time of any component a temperature dependence similar to that of $CaWO_4$ or $SrWO_4$ as shown in Fig. 4.9. For this reason, the following analysis could not be done for $BaWO_4$.

Figure 4.9 presents the temperature dependence of the decay time of the intrinsic luminescence of $SrWO_4$ and $CaWO_4$. The $CaWO_4$ curve corresponds to a typical behavior of the triplet state. The low and high temperature plateaus are determined by k_1 and k_2. The position and slope of the intermediate region are determined by Δ_{SOC} and K. It is seen that for $SrWO_4$ neither plateau is present. The reason for the low temperature behavior is that even at 2 K there is considerable contribution from the k_{12} transitions due to the small value of Δ_{SOC}, which does not allow the lower lying metastable level to become dominant, which would otherwise lead to the plateau. The high temperature plateau is never reached because of an early onset of thermal quenching, which can also be seen from the temperature dependence of the intensity of the main emission. The latter

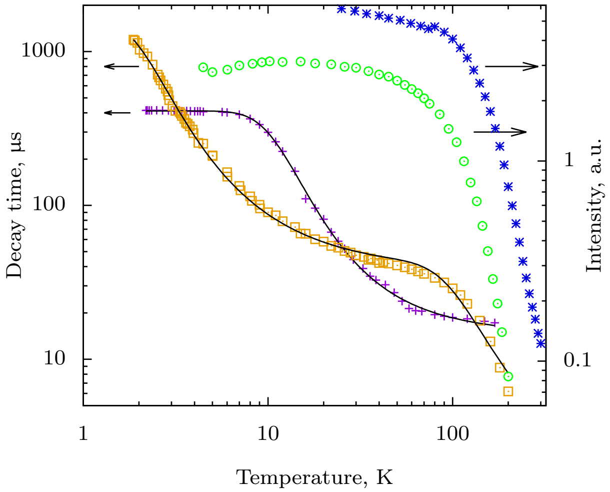

Figure 4.9: Decay time temperature dependence of the intrinsic emission of $SrWO_4$ (squares) and $CaWO_4$ (crosses) and the temperature dependence of the intensity of the intrinsic (stars) and extrinsic (circles) emission of $SrWO_4$. Solid lines are fits to the model [Eq. (2.20)]. Logarithmic scale is chosen for better visualization.

is similar to the temperature dependence of the intensity of the green emission.

We fitted the curves with the model of triplet excitons [Eq. (2.20)]; the results are shown in Table 4.2. Since neither plateau is present for $SrWO_4$, its k_1 and k_2 values contain considerable uncertainty. The rest of the fitting parameters are much more insensitive to data point errors. Also, since the temperature range for $CaWO_4$ was below the onset of thermal quenching, its E_x and K_x values are taken from [68].

The temperature dependencies of both the intensity of main emission and its decay time (Fig. 4.9 and Fig. 11 from [69]) suggest that the thermal diffusion of excitons is stronger in $SrWO_4$ than in $CaWO_4$ for the following reasons. Firstly, the luminescence quenching, supposedly due to diffusion, starts at a much

Table 4.2: Three level model parameters for $CaWO_4$ and $SrWO_4$.

	$CaWO_4$	$SrWO_4$
k_1	$2.4 \times 10^3\,s^{-1}$	$5.9 \times 10^2\,s^{-1}$
k_2	$1.1 \times 10^5\,s^{-1}$	$2 \times 10^5\,s^{-1}$
K	$1.3 \times 10^5\,s^{-1}$	$1.4 \times 10^4\,s^{-1}$
Δ_{SOC}	4.2 meV	0.8 meV
K_x	$8.6 \times 10^9\,s^{-1}$ [68]	$8.1 \times 10^5\,s^{-1}$
E_x	320 meV [68]	36 meV

lower temperature in $SrWO_4$ (36 meV) than in $CaWO_4$ (320 meV). Secondly, the effect of spin-orbit interaction (SOC) is less in $SrWO_4$ (0.8 meV) than in $CaWO_4$ (4.2 meV). It follows that the electron spends less time in the vicinity of W in $SrWO_4$. Defining the spread of the exciton wavefunction as the effective exciton radius, we may conclude that $SrWO_4$ has a larger exciton radius, which presumably enhances exciton diffusion. We stress that such a definition is merely for convenience and should not be confused with the exciton Bohr radius, a term that is only applicable to Wannier-Mott excitons. In tungstates, the hole and electron components of the exciton are localized on O and W atoms, respectively, the resulting wavefunction of which has far from spherical symmetry.

Assuming that thermal diffusion correlates with the exciton radius, it can be explained why it is difficult to see any intrinsic luminescence in $BaWO_4$. If the exciton radius, and thus diffusion, increases in the order $CaWO_4 \rightarrow SrWO_4 \rightarrow BaWO_4$, then it could be that already at 4.2 K the intrinsic luminescence of $BaWO_4$ is quenched to a degree that only defect luminescence is observable.

A relation between the Frenkel exciton radius and its dipole moment has thus far not been established. It is possible that a greater delocalization of the exciton with possibly larger hybridization with cation states leads to a greater dipole moment of the exciton for transitions between the exciton state and the WO_4^{2-} ground state, and also to a greater dipole moment for exciton ionization. With such a scenario we expect the dipole-dipole interaction radius to increase in the order $CaWO_4 \rightarrow SrWO_4 \rightarrow BaWO_4$, since a greater dipole moment leads to a greater efficiency of FRET [70]. In Sec. 4.1, the $R_{\text{d-d}}$ values of $CaWO_4$ and $SrWO_4$ were determined to be 3.17 nm and 5.84 nm, respectively. The efficiency of FRET thus seems to correlate with the exciton radius. By extrapolation, we would expect $BaWO_4$ to have the largest $R_{\text{d-d}}$ of the crystals.

Ground state electron and hole localization. While we have thus shown that a larger cation radius leads to a larger exciton radius, the reason for this is not clear. Despite the differences in luminescence properties, the electronic structure, in the energy range of interest, is remarkably similar for the crystals, with no cation states near the top of the valence band (VB) or the bottom of the conduction band (CB) [71]. The VB is 4–5 eV wide and consists mainly of O 2p states with some contribution from the W 5d e and t_2-like states in the lower half. The bottom of the CB is comprised of W 5d e-like states, followed by a small gap. The main effect of the cation seems to be on the unit cell parameters. It follows that the stark contrast in the luminescence properties of these crystals, which we believe to originate from the different exciton radii, cannot be explained in terms of ground state properties, but is instead attributed to the different extent of electron-hole correlation and/or the excited state geometry relaxation and the resulting autolocalization of the exciton.

To further test this claim, we estimated the localization lengths of the valence and conduction states in the ground state configuration. In order to explain the observed spectra and the decay kinetics, we would expect the valence and/or conduction electrons to become drastically more delocalized in the order $CaWO_4$ → $BaWO_4$. The localization lengths can be calculated using maximally localized Wannier functions [72, 73]. Wannier functions are the real-space equivalent of Bloch functions for representing the electronic structure of a solid. A set of N generalized Wannier functions is defined via Bloch functions as

$$w_{n,\boldsymbol{R}}(\boldsymbol{r}) = \frac{V}{(2\pi)^3} \int_{\mathrm{BZ}} e^{-i\boldsymbol{k}\boldsymbol{R}} \sum_{m=1}^{N_{\boldsymbol{k}}} U_{mn}^{\boldsymbol{k}} \psi_{m,\boldsymbol{k}}(\boldsymbol{r})\, \mathrm{d}\boldsymbol{k}, \tag{4.3}$$

where $N_{\boldsymbol{k}}$ is the number of bands within an energy window of interest and V is the unit cell volume. The $U_{mn}^{\boldsymbol{k}}$ are only required to be unitary, leaving much freedom in the construction of Wannier functions. Two physically equivalent sets of Wannier functions could have very different spatial extents. However, there exists a special set with a minimal spatial spread Ω, defined as

$$\Omega = \sum_{n=1}^{N} \left[\langle w_{n,\boldsymbol{0}} | \, r^2 \, | w_{n,\boldsymbol{0}} \rangle - \langle w_{n,\boldsymbol{0}} | \, \boldsymbol{r} \, | w_{n,\boldsymbol{0}} \rangle^2 \right]. \tag{4.4}$$

An efficient method for minimizing Ω is the Marzari-Vanderbilt scheme [72], which for a given set of Bloch functions and energies from a uniform mesh of $\boldsymbol{k}$-points produces the $U_{mn}^{\boldsymbol{k}}$ required to construct MLWFs. If the bands of interest form an isolated group, such as the valence bands of $CaWO_4$, $N_{\boldsymbol{k}} = N$ in Eq. (4.3). If this is not the case, such as the conduction bands of $CaWO_4$, an additional disentanglement procedure must be performed before minimizing the spread Ω [73]. The Wannier functions thus constructed span the same portion of the Hilbert space as the underlying Bloch functions.

Using the formalism of MLWFs, the localization length can be defined as

$$\delta_n = \sqrt{\langle w_{n\boldsymbol{0}} | r^2 | w_{n\boldsymbol{0}} \rangle - \langle w_{n\boldsymbol{0}} | \boldsymbol{r} | w_{n\boldsymbol{0}} \rangle^2} \tag{4.5}$$

for a given Wannier function $w_{n\boldsymbol{0}}(\boldsymbol{r})$. The Bloch states entering Eq. (4.3) are generally approximated by the Kohn-Sham states obtained from a DFT calculation. Our DFT calculations were performed with Abinit [74] within the PAW [75] formalism using the PBEsol [76] exchange-correlation functional. The calculated DOS and band structures (not shown) agreed well with previous results [23, 77, 71] and, together with the optimized lattice constants (Table 2.1), attest to the accuracy of the generated PAW datasets.

For tungstates, there are two formula units in the unit cell and thus a total of 48 valence electrons. From the shape of the MLWFs (Fig. 4.10), the upper half of the VB has purely p_π character, in agreement with [23]. The lower half is formed

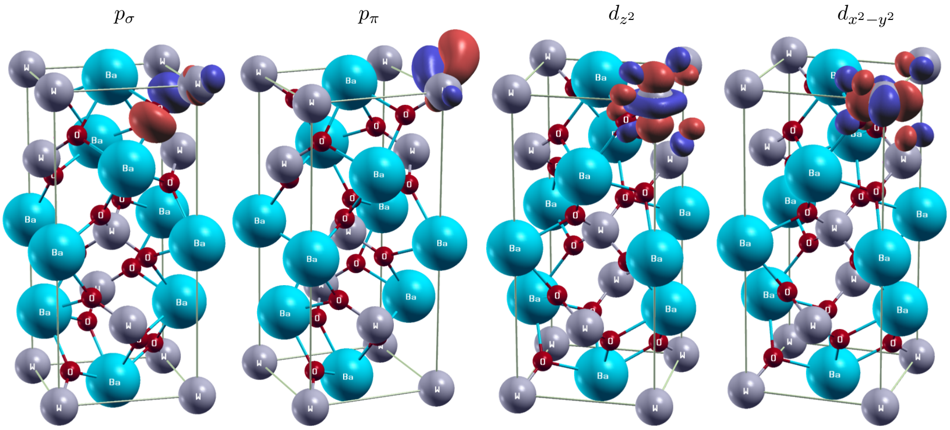

Figure 4.10: MLWFs corresponding to the valence and the lowest conduction bands of $BaWO_4$. Out of the total of 48 valence and 8 conduction states, only the distinct ones are shown. The rest have a similar shape but are located at different atoms with different orientations. The red and blue isosurfaces correspond to the positive and negative values of the wavefunction at the isovalue of $5.2\,\text{Å}^{-1.5}$.

Table 4.3: The localization lengths [Eq. (4.5)] for the (mainly) O 2p derived valence band and the W 5d derived conduction band states in Å. The results are shown only for the optimized geometry (Table 2.1), although similar results were also obtained for the experimental lattice parameters.

	valence band		conduction band	
	$32 \times p_\sigma$	$16 \times p_\pi$	$4 \times d_{z^2}$	$4 \times d_{x^2-y^2}$
$CaWO_4$	1.09	1.07	1.75	1.86
$SrWO_4$	1.12	1.06	1.78	1.86
$BaWO_4$	1.19	1.07	1.91	2.01

Table 4.4: Physical parameters of $CdWO_4$ as required by Eqs. (2.28) and (2.30). The maximum scintillator yield taken from the high-energy part of the experimental data is 15 800 ph/MeV, which according to Eq. (2.25) is equal to χ/E_{eh}.

$R_{\text{d-d}}$	3.7 nm (present work)
V	149 Å^3
χ/E_{eh}	15 800 MeV^{-1} [7]
I	468.3 eV [78]
r_{tr}^{nonrel}	4.5 nm (fit)
r_{tr}^{rel}	4.7 nm (fit)

of p_σ bonds hybridized with 5d e and t_2-like states. The 8 conduction states have the 5d e-like character. It is evident (Table 4.3) that the valence and conduction states indeed become slightly more delocalized as the cation radius increases, but not enough to explain the observed experimental results. The differences in δ are similar to the differences in the lattice constants. That the localization length of the p_π states remains the same is understood by the fact that these are more localized inside the tetrahedral WO_4^{2-} molecular complex. The W-O bond length and thus the WO_4^{2-} dimensions are the same for these crystals (Table 2.1).

We conclude that indeed no ground state calculation is able to explain the radically different thermal stabilities or the differences in the $R_{\text{d-d}}$ values. These must come entirely from the differences in the excited state dynamics in these crystals. It is possible that after relaxation a larger cation radius leads to a greater hybridization between the cation and the exciton state, causing the exciton wavefunction to have a larger spread, which would explain the correlation between the cation radius, exciton radius, and the dipole-dipole interaction radius.

4.4 Modeling nonproportionality of $CdWO_4$

We have applied the models developed in Sec. 2.4 to $CdWO_4$ using the parameters of Table 4.4 and the experimental nonproportionality curve of [7]. We note that although the experimental data account for photon-nonproportionality while Eqs. (2.28) and (2.30) describe electron-nonproportionality, the two quantities are very similar at high energies (above K-shell binding energies or 70 keV for $CdWO_4$).

If we estimate the average energy required for exciton formation to be $E_{eh}/\chi = 63.3$ eV and take $E_{eh} = 2.5 \times E_g = 12.5$ eV, then $\chi = 0.20$, which shows that 80% of all e-h pairs do not form excitons but are trapped or recombine nonradiatively. The thermalization distance of such electrons can extend to hundreds on nanometers [44]. Slow recombination of trapped charge carriers

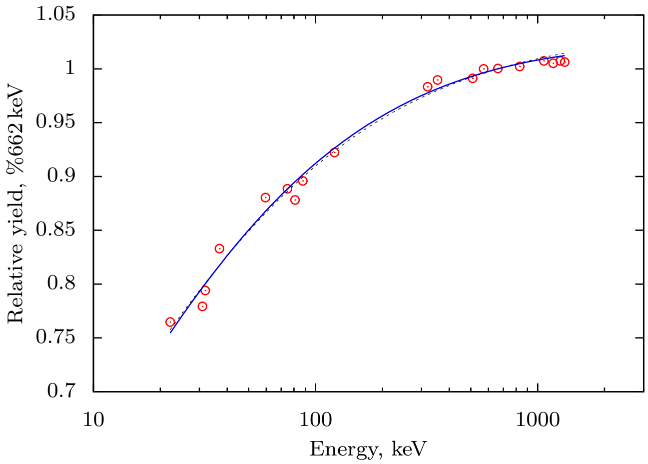

Figure 4.11: Scintillator yield of $CdWO_4$ at RT normalized to the value at 662 keV. Symbols are the experimental data [7], solid line is a fit with Eq. (2.28), dotted line is a fit with Eq. (2.30). The relativistic formula produces a slightly better fit.

resulting in afterglow is not included in the present models.

The track radii, as calculated with Eqs. (2.28) and (2.30), are 4.7 and 4.5 nm, respectively. There is little difference in the radii or in the fits to the model (Fig. 4.11), showing that the two approximations made with Eq. (2.30) are well justified. The first one was the average ionization potential approximation, which requires $E \gg I_i$ and influences only the low-energy part of the nonproportionality curve. Even though the highest I_i is due to the W 1s orbitals (70 keV), most of the contribution to the stopping power is actually from the outer shells, which have bigger weights in Eq. (2.28). For most electron shells in the system, $I_i < 10\,\text{keV}$, which is less than the lowest energy data point in Fig. 4.11. The averaging of I_i is thus a good approximation for the whole data range. The second approximation was the nonrelativistic regime, i.e., $E \ll 2mc^2$, which influences mainly the high-energy region. The fact that the curves almost coincide also in the high-energy region allows us to conclude that the crystal becomes proportional before relativistic effects become important.

The fact that the simplified model [Eq. (2.30)] is just as accurate as the full solution [Eq. (2.28)] for $CdWO_4$, and presumably for other tungstates, is significant because the latter is about two orders of magnitude more expensive.

We note that the current models do not account for electron exchange between the secondary particles in the track. Including exchange would modify the factor 4 under the logarithm in Eq. (2.30) to $\sqrt{e/2}$ [43] and reduce the track radius to 3.9 nm [16].

4.5 Quasiparticle band structure of $CdWO_4$

We have calculated the quasiparticle band structure of $CdWO_4$ in the G_0W_0 approximation. The calculations were performed with Abinit [74] within the all-electron PAW [75] formalism using the PBEsol [76] exchange-correlation functional. The PAW method is an accurate alternative to the commonly used pseudopotential approximation, which tends to overestimate band gaps compared to all-electron approaches in QP calculations [79]. Details about the construction of PAW datasets in order to be sufficiently accurate for QP calculations are given in [80]. Here we only demonstrate the accuracy of the datasets for ground state calculations by comparing the calculated lattice constants to the experimental ones (Table 4.5).

Table 4.5: Atom positions in the unit cell of $CdWO_4$. Cd sites are located at $\pm(1/2, y, 3/4)$, W sites at $\pm(0, y, 1/4)$ and O_i sites at $\pm(x_i, y_i, z_i)$ and $\pm(x_i, -y_i, z_i + 1/2)$ for $i = 1,2$.

	Experimental at RT [81]			Calculated at 0 K		
a(Å)	5.0289			5.0141		
b(Å)	5.8596			5.8953		
c(Å)	5.0715			5.0508		
β(deg)	91.519			91.136		
V(Å^3)	149.39			149.27		
	x	y	z	x	y	z
Cd	0.5	0.3027	0.75	0.5	0.3057	0.75
W	0.0	0.17847	0.25	0.0	0.1767	0.25
O_1	0.242	0.372	0.384	0.243	0.368	0.387
O_2	0.202	0.096	0.951	0.204	0.095	0.950

A convergence study was required for each summation index in the expressions for the matrix elements [Eqs. (2.40) and (2.41)]. The convergence criterion for each parameter tested was chosen to be 10 meV in the QP energies. This should ensure that the final uncertainties are dominated by the theoretical accuracy of the G_0W_0 method itself. The converged calculation was performed at a plane wave cutoff of 626 eV, using 1536 empty states in the calculation of W and 1536 states in the calculation of the matrix elements of Σ^c. The dimension of the W matrix in terms of the energy of $\boldsymbol{G}$-vectors was 326 eV (2013 plane waves). The energy cutoff for the matrix elements of Σ^x was 5440 eV (136 247 plane waves) for the Cd 4d states and 1632 eV (28 193 plane waves) otherwise. An unshifted $4 \times 4 \times 4$ grid was used for Brillouin zone sampling (BZS). Detailed information about the convergence studies is found in the supplementary material of [80].

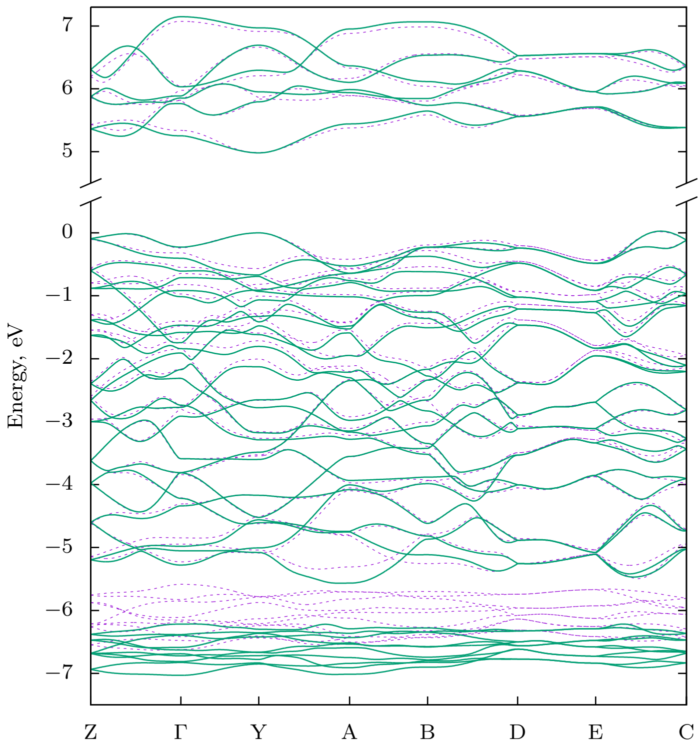

Figure 4.12: QP (solid) and KS (dotted) band structures of $CdWO_4$. A scissor shift of 1.91 eV (see the end of Sec. 2.5) is include in the KS band structure. In reality, the conduction bands are not isolated, only the first 6 bands are shown here. Coordinates of the BZ points are given in [84].

Once the QP energies are calculated on a uniform $\boldsymbol{k}$-mesh, the full band structure can be interpolated using a technique based on Maximally localized Wannier functions as detailed in [53]. The basic idea is similar to the Slater-Koster interpolation method [82], except that here the tight-binding matrix elements are calculated from first principles as opposed to being adjustable parameters. The Wannier interpolation of the QP band structure was performed with the Wannier90 package [83].

The QP band structure is shown in Fig. 4.12 along with the KS band structure, where the scissor shift is chosen to match the QP band gap. To our knowledge, there are no prior calculations of the full QP band structure for such complex crystals as tungstates. The KS band structure agrees well with previous calculations [24, 84]. In the vicinity of the conduction band minimum or the valence band maximum, the bands are similar for both cases, but further away the position and shape of the KS bands starts differing from the QP results. The second highest group of valence bands, derived from the Cd 4d states, is misplaced

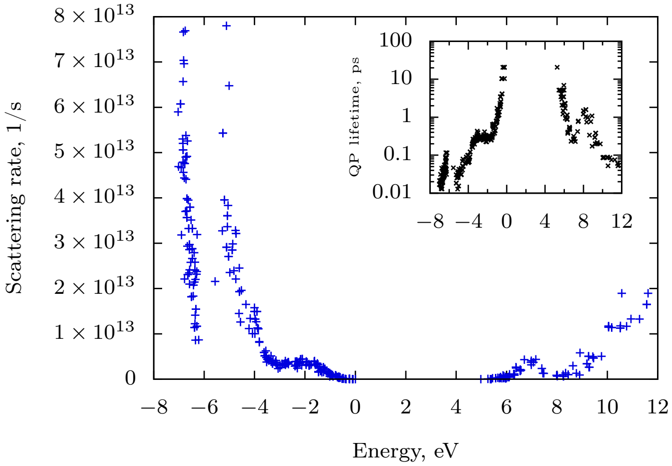

Figure 4.13: Electron-electron scattering rate in $CdWO_4$ as calculated according to Eq. (2.38). Inset shows the quasiparticle lifetimes.

by 0.5 eV in DFT. The direct band gap minimum, located at the Y-point, is 5.0 eV in the G_0W_0 approximation and 3.1 eV in DFT.

All calculations have been performed in the nonrelativistic regime. However, due to the presence of Cd and W, spin-orbit coupling cannot be completely neglected. Since the QP corrections and SOC can be considered independent perturbations, it suffices to estimate the effects of SOC in DFT only. We have calculated the KS band structure including SOC (not shown) within the PAW formalism as implemented in Abinit. This modifies the KS energies by no more than about 0.1 eV, except for the Cd 4d bands which are split in two, in agreement with [24]. The band gap energy is reduced by 44 meV, which corrects the G_0W_0 band gap to slightly below 5 eV. Taking the optical gap from the Urbach tail analysis as 4.8 eV [16, 28], comparing this to the calculated single-particle G_0W_0 band gap and considering the accuracy of the methods used, we propose an upper bound of 0.4 eV for the exciton binding energy in $CdWO_4$. For comparison, the exciton binding energies in $PbWO_4$ and the structurally similar $ZnWO_4$ have been estimated to be ~ 0.1 eV [85] and 0.53 eV [86], respectively.

Figure 4.13 presents the energy dependence of the electron-electron scattering rate. Near the band extrema the scattering rate nears zero and accordingly the quasiparticle lifetime becomes infinite, as it should in the Fermi liquid theory. Further away the scattering increases, which can be interpreted as an increasing loss of the single-particle character. The classical phase space argument would result in the $1/\tau^{\mathrm{QP}} \propto |\varepsilon - \varepsilon_F|^2$ dependence. For $CdWO_4$, the dependence seems to be much more complex. In particular, the feature at -7 eV, which is due to the Cd 4d states, shows a very sharp slope in the scattering rate and consequently in the QP lifetimes.

The electron-phonon scattering rate has not yet been determined for $CdWO_4$. However, it has been determined for the scintillators of NaI, CsI, CaF_2, and BaF_2, where the LO phonon creation and annihilation rates are on the order of 10^{14} or higher in a wide energy range [44]. Since the thermalization stage in $CdWO_4$ has been estimated to be faster than in those crystals [12], we expect the electron-phonon scattering rates to be at least as high. The energy range relevant for thermalization is determined by the energy distance of $E_g = 5\,\mathrm{eV}$ from the band extrema, or $-5\ldots10\,\mathrm{eV}$ in Fig. 4.13. Only the electrons and holes with those energies would be present in the crystal at the beginning of thermalization. In that energy region, the electron-electron scattering rate is less than $3\times10^{13}\,\mathrm{s}^{-1}$, which is much less than the estimated electron-phonon scattering rate. We may conclude that the electron-electron scattering rate is sufficiently small and the quasiparticles sufficiently stable that if suffices to describe thermalization only in terms of the electron-phonon scattering, as has been done in most studies on modeling scintillator thermalization so far [21, 44].

Chapter 5

CONCLUSIONS

In this work, we have studied the excited state dynamics under high excitation density conditions in the tungstate scintillators. We have developed and tested several models covering different stages of the scintillation process, which include excitation, thermalization, and the luminescence stage.

Under excitation by femtosecond laser pulses with sub-band-gap photon energies, we have discovered an absorption saturation effect, which is explained in terms of a limited number of centers having the correct atomic configuration for absorbing a photon at the moment of excitation. The saturation densities (limits to the exciton density in the crystal) were determined for $CdWO_4$, $CaWO_4$, and $SrWO_4$ by fitting experimental data to the model. The temperature and energy dependencies of the saturation density agreed with the model predictions.

Based on previous works, we have further developed the theory of nonlinear quenching of exciton luminescence by introducing a model that accounts for both absorption saturation and the dipole-dipole interaction (FRET) of excitons. The model was successfully fitted with experimental data for determining the dipole-dipole interaction radii for selected tungstates.

In addition to studying the nonlinear effects of exciton luminescence, we have determined several exciton characteristics from low excitation density experiments and found a correlation between the cation radius, exciton radius, and the dipole-dipole interaction radius. A strong variation in those quantities was found in the series $CaWO_4$, $SrWO_4$, $BaWO_4$. The result is surprising due to the similar ground state structural and electronic properties of these crystals and leads us to hypothesize that the excited state structural relaxation could be sensitive to the properties of the cation for reasons not yet understood.

A model of nonproportionality for intrinsic excitonic scintillators was developed. The model was successfully tested on experimental data and produced a track radius of 4.6 nm for $CdWO_4$. We confirmed the validity of both the average ionization potential approximation and the nonrelativistic regime for the modeling of nonproportionality.

The contribution of electron-electron scattering to thermalization was investigated by calculating the excited state quasiparticle lifetimes in the G_0W_0 approximation. Based on general considerations and the results of the calculation we were able to conclude that the rate of electron-electron scattering is negligible compared to the rate of electron-phonon scattering, which dominates thermalization.

Chapter 6

SUMMARY IN ESTONIAN

Ergastatud seisundite dünaamika kõrge ergastustiheduse tingimustes volframaatides

Antud töös uuritakse ergastatud seisundite dünaamikat kõrge ergastustiheduse tingimustes volframaadi stsintillaatorkristallides. Me oleme tuletanud ja rakendanud mitmeid mudeleid, mis katavad erinevaid stsintillatsiooni protsessi staadiume, s.h. ergastamise, termilisatsiooni ja luminestsentsi staadiumid.

Ergastamisel fs laserimpulssidega keelutsooni energiast madalamate energiatega footonitega oleme avastanud neeldumise küllastumise efekti, mida saab seletada lõpliku arvu tsentrite leidumisega kristallis ergastamise hetkel, millede aatomite konfiguratsioon on sobilik footoni neelamiseks. Kohandades mudelit eksperimentaalsete andmetega oleme leidnud küllastumise tihedused (maksimaalsed lubatud eksitonitihedused kristallis) $CdWO_4$, $CaWO_4$ ja $SrWO_4$ kristallide jaoks. Küllastustiheduste temperatuuri- ja energiasõltuvused lähevad kokku mudeli ennustustega.

Lähtudes varasematest töödest oleme arendanud edasi mittelineaarse eksitonluminestsentsi kustumise teooriat luues uue mudeli, mis arvestab nii neeldumise küllastumise kui dipool-dipool interaktsiooniga (FRET) eksitonide vahel. Mudelit õnnestus edukalt lähendada eksperimentaalsete andmetega leidmaks dipool-dipool interaktsiooni raadiust volframaatide jaoks.

Lisaks mittelineaarsete efektide uurimisele eksitonluminestsentsi põhjal oleme uurinud eksitoni karakteristikuid madala ergastustiheduse tingimustes ja leidnud korrelatsiooni katiooni raadiuse, eksitoni raadiuse ja dipool-dipool interaktsiooni raadiuse vahel. Nimetatud suuruste jaoks leiti suur varieeruvus reas $CaWO_4$, $SrWO_4$, $BaWO_4$. Tulemus on üllatav arvestades nende kristallide sarnaseid kristall- ja elektronstruktuure ning lubab oletada, et ergastatud seisundi relaksatsioon on tundlik katiooni omaduste suhtes siiani arusaamata põhjustel.

Arendasime mitteproportsionaalsuse mudeli eksitonkiirgusel põhinevate stsintillaatorite jaoks. Mudeli edukas testimine eksperimentaalandmete peal lubas leida kõrge energia osakese trajektoori raadiuse väärtuseks 4.6 nm $CdWO_4$

kristallis. Lisaks kinnitasime keskmistatud ionisatsioonipotentsiaali lähenduse ja mitterelativistliku režiimi kasutamise korrektsust mitteproportsionaalsuse mudelites. Hindasime elektron-elektron hajumise osakaalu termilisatsiooni faasis arvutades ergastatud seisundi kvaasiosakeste eluead G_0W_0 lähenduses. Lähtudes üldistest kaalutlustest ja kalkulatsiooni tulemustest võime järeldada, et elektron-elektron hajumise osakaal on tühine võrreldes elektron-foonon hajumisega termilisatsiooni ajal. Viimane on reeglina domineeriv.

ACKNOWLEDGMENTS

This work was supported in part by the Access to Research Infrastructures activity in the FP6 of the EU under contract RII3-CT-2003-506350, Laserlab Europe, by the Estonian Science Foundation under grant 8893, by the institutional research funding IUT (IUT02-26) of the Estonian Ministry of Education and Research, and by the Graduate School "Functional materials and technologies" receiving funding from the European Social Fund under project 1.2.0401.09-0079 in Estonia. The financial support from Mobilitas ESF program (grant MTT83) and LASERLAB-EUROPE (grant agreement no. 284464, EC's Seventh Framework Programme), is also gratefully acknowledged. The quasiparticle calculations were carried out at the High Performance Computing Center of the University of Tartu.

REFERENCES

[1] T. A. Edison, Nature (London) **53**, 470 (1896).

[2] W. W. Moses, in V. V. Mikhailin, editor, *SCINT99: Proc. Int. Conf. on Inorganic Scintillators and Their Applications*, pages 11–20, Lomonosov Moscow State University, Moscow (1999).

[3] L. Nagornaya, G. Onyshchenko, E. Pirogov, N. Starzhinskiy, I. Tupitsyna, V. Ryzhikov, Y. Galich, Y. Vostretsov, S. Galkin, and E. Voronkin, Nucl. Instr. Meth. Phys. Res. A **537**, 163 (2005).

[4] C. Arnaboldi, J. Beeman, O. Cremonesi, L. Gironi, M. Pavan, G. Pessina, S. Pirro, and E. Previtali, Astropart. Phys. **34**, 143 (2010).

[5] S. Cebrián, N. Coron, G. Dambier, P. de Marcillac, E. García, I. Irastorza, J. Leblanc, A. Morales, J. Morales, A. O. de Solórzano, J. Puimedón, M. Sarsa, and J. Villar, Phys. Lett. B **563**, 48 (2003).

[6] F. Petricca, G. Angloher, C. Cozzini, T. Frank, D. Hauff, J. Ninković, F. Pröbst, W. Seidel, and S. Uchaikin, Nucl. Instr. Meth. Phys. Res. A **520**, 193 (2004).

[7] W. Klamra, T. Szczesniak, M. Moszynski, J. Iwanowska, L. Swiderski, A. Syntfeld-Kazuch, V. N. Shlegel, Y. V. Vasiliev, and E. N. Galashov, J. Instrum. **7**, P03011 (2012).

[8] R.-Y. Zhu, IEEE Trans. Nucl. Sci. **51**, 1560 (2004).

[9] J. Šulc, H. Jelinková, T. Basiev, M. Doroschenko, L. Ivleva, V. Osiko, and P. Zverev, Opt. Mater. **30**, 195 (2007).

[10] J. Singh, J. Appl. Phys. **110**, 024503 (2011).

[11] G. Bizarri, W. W. Moses, J. Singh, A. N. Vasil’ev, and R. T. Williams, J. Appl. Phys. **105**, 044507 (2009).

[12] J. Q. Grim, K. B. Ucer, A. Burger, P. Bhattacharya, E. Tupitsyn, E. Rowe, V. M. Buliga, L. Trefilova, A. Gektin, G. A. Bizarri, W. W. Moses, and R. T. Williams, Phys. Rev. B **87**, 125117 (2013).

[13] M. Kirm, V. Nagirnyi, E. Feldbach, M. D. Grazia, B. Carré, H. Merdji, S. Guizard, G. Geoffroy, J. Gaudin, N. Fedorov, P. Martin, A. N. Vasil'ev, and A. Belsky, Phys. Rev. B **79**, 233103 (2009).

[14] V. Nagirnyi, S. Dolgov, R. Grigonis, M. Kirm, L. L. Nagornaya, F. Savikhin, V. Sirutkaitis, S. Vielhauer, and A. N. Vasil'ev, IEEE Trans. Nucl. Sci. **57**, 1182 (2010).

[15] A. N. Vasil'ev, IEEE Trans. Nucl. Sci. **55**, 1054 (2008).

[16] R. Laasner, N. Fedorov, R. Grigonis, S. Guizard, M. Kirm, V. Makhov, S. Markov, V. Nagirnyi, V. Sirutkaitis, A. Vasil'ev, S. Vielhauer, and I. A. Tupitsyna, J. Phys.: Condens. Matter **25**, 245901 (2013).

[17] S. Vielhauer, V. Babin, M. D. Grazia, E. Feldbach, M. Kirm, V. Nagirnyi, and A. Vasil'ev, Phys. Sol. State **50**, 1789 (2008).

[18] T. H. Keil, Phys. Rev. **144**, 582 (1966).

[19] B. Sadigh, P. Erhart, D. Åberg, A. Trave, E. Schwegler, and J. Bude, Phys. Rev. Lett. **106**, 027401 (2011).

[20] R. Laasner, V. Nagirnyi, S. Vielhauer, M. Kirm, D. Spassky, V. Sirutkaitis, R. Grigonis, and A. N. Vasil'ev, J. Phys.: Condens. Matter. (2015), accepted.

[21] A. N. Vasil'ev and A. V. Gektin, IEEE Trans. Nucl. Sci. **61**, 235 (2014).

[22] A. W. Sleight, Acta Crystallogr. Sec. B **28**, 2899 (1972).

[23] Y. Zhang, N. A. W. Holzwarth, and R. T. Williams, Phys. Rev. B **57**, 12738 (1998).

[24] Y. Abraham, N. A. W. Holzwarth, and R. T. Williams, Phys. Rev. B **62**, 1733 (2000).

[25] G. Blasse and W. J. Schipper, phys. stat. sol. (a) **25**, K163 (1974).

[26] R. Grasser, A. Scharmann, and K.-R. Strack, J. Lumin. **27**, 263 (1982).

[27] M. J. J. Lammers, G. Blasse, and D. S. Robertson, phys. stat. sol. (a) **63**, 569 (1981).

[28] V. Nagirnyi, M. Kirm, A. Kotlov, A. Lushchik, and L. Jönsson, J. Lumin. **102**, 597 (2003).

[29] V. Nagirnyi, E. Feldbach, L. Jönsson, M. Kirm, A. Kotlov, A. Lushchik, V. A. Nefedov, and B. I. Zadneprovski, Nucl. Instr. Meth. Phys. Res. A **486**, 395 (2002).

[30] M. Itoh, H. Yokota, M. Horimoto, M. Fujita, and Y. Usuki, phys. stat. sol. (b) **231**, 595 (2002).

[31] V. Hizhnyakov, phys. stat. sol. (b) **158**, 725 (1990).

[32] R. T. Williams, J. Q. Grim, Q. Li, K. B. Ucer, and W. W. Moses, phys. stat. sol. (b) **248**, 426 (2011).

[33] V. Nagirnyi, G.Geoffroy, R.Grigonis, S.Guizard, M.Kirm, A.Kotlov, L.L.Nagornaya, M. Nikl, V.Sirutkaitis, and S.Vielhauer, Rad. Meas. **45**, 262 (2010).

[34] https://raullaasner.github.io/gadfit (2015).

[35] D. W. Marquardt, J. Soc. Indust. Appl. Math. **11**, 431 (1963).

[36] E. Gürmen, E. Daniels, and J. S. King, J. Chem. Phys. **55**, 1093 (1971).

[37] R. Grasser, E. Pitt, A. Scharmann, and G. Zimmerer, phys. stat. sol. (b) **69**, 359 (1975).

[38] M. Nikl, V. V. Laguta, and A. Vedda, phys. stat. sol. (b) **245**, 1701 (2008).

[39] V. Mürk, M. Nikl, E. Mihoková, and K. Nitsch, J. Phys.: Condens. Matter. **9**, 249 (1997).

[40] N. F. Mott, Proc. R. Soc. Lond. A **167**, 384 (1938).

[41] J. Singh and R. T. Williams, editors, *Excitonic and Photonic Processes in Materials*, Springer-Verlag Singapur, 1 edition (2015), ISBN 978-981-287-131-2.

[42] I. V. Khodyuk, M. S. Alekhin, J. T. de Haas, and P. Dorenbos, Nucl. Instrum. Meth. A **642**, 75 (2011).

[43] A. Jablonski, S. Tanuma, and C. J. Powell, Surf. Interface Anal. **38**, 76 (2006).

[44] Z. Wang, Y. Xie, L. W. Campbell, F. Gao, and S. Kerisit, J. Appl. Phys. **112**, 014906 (2012).

[45] L. Landau, E. M. Lifshitz, and L. P. Pitaevskii, *Statistical physics*, volume 2 of *Course of Theoretical Physics*, Pergamon Press, Oxford, 1 edition (1980).

[46] M. S. Hybertsen and S. G. Louie, Phys. Rev. B **34**, 5390 (1986).

[47] W. G. Aulbur, L. Jönsson, and J. W. Wilkins, Solid State Phys. **54**, 1 (1999).

[48] M. van Schilfgaarde, T. Kotani, and S. Faleev, Phys. Rev. Lett. **96**, 226402 (2006).

[49] S. V. Faleev, M. van Schilfgaarde, and T. Kotani, Phys. Rev. Lett. **93**, 126406 (2004).

[50] A. Marini, G. Onida, and R. D. Sole, Phys. Rev. Lett. **88**, 016403 (2002).

[51] P. Echenique, J. Pitarke, E. Chulkov, and A. Rubio, Chem. Phys. **251**, 1 (2000).

[52] M. S. Hybertsen and S. G. Louie, Phys. Rev. B **32**, 7005 (1985).

[53] D. R. Hamann and D. Vanderbilt, Phys. Rev. B **79**, 045109 (2009).

[54] L. Hedin, Phys. Rev. **139**, A796 (1965).

[55] S. Lebègue, B. Arnaud, M. Alouani, and P. E. Bloechl, Phys. Rev. B **67**, 155208 (2003).

[56] J. P. Perdew and M. Levy, Phys. Rev. Lett. **51**, 1884 (1983).

[57] L. J. Sham and M. Schlüter, Phys. Rev. Lett. **51**, 1888 (1983).

[58] S. Markov, V. Nagirnyi, A. Vasil'ev, V. Makhov, R. Laasner, S. Vielhauer, M. Kirm, R. Grigonis, and V. Sirutkaitis, Cent. Eur. J. Phys. **10**, 1002 (2012).

[59] S. Chernov, R. Deych, L. Grigorjeva, and D. Millers, Mater. Sci. Forum **239**, 299 (1997).

[60] M. Fujita, M. Itoh, T. Katagiri, D. Iri, M. Kitaura, and V. B. Mikhailik, Phys. Rev. B **77**, 155118 (2008).

[61] J. B. Khurgin, Phys. Rev. B **77**, 235206 (2008).

[62] R. Deych, J. Dobbs, S. Marcovici, and B. Tuval, in P. Dorenbos and C. W. E. van Eijk, editors, *SCINT95: Proc. Int. Conf. on Inorganic Scintillators and Their Applications*, pages 36–39, Delft University Press, Delft, The Netherlands (1995).

[63] V. Kolobanov, I. Kamenskikh, V. Mikhailin, I. Shpinkov, D. Spassky, B. Zadneprovsky, L. Potkin, and G. Zimmerer, Nucl. Instr. Meth. Phys. Res. A **486**, 496 (2002).

[64] V. Babin, P. Bohacek, E. Bender, A. Krasnikov, E. Mihokova, M. Nikl, N. Senguttuvan, A. Stolovits, Y. Usuki, and S. Zazubovich, Rad. Meas. **38**, 533 (2004).

[65] R. Grasser and A. Scharmann, J. Lumin. **12**, 473 (1976).

[66] R. Lacomba-Perales, J. Ruiz-Fuertes, D. Errandonea, D. Martínez-García, and A. Segura, Europhys. Lett. **83**, 37002 (2008).

[67] M. Nikl, P. Bohacek, E. Mihokova, M. Kobayashi, M. Ishii, Y. Usuki, V. Babin, A. Stolovich, S. Zazubovich, and M. Bacci, J. Lumin. **87**, 1136 (2000).

[68] V. B. Mikhailik, H. Kraus, S. Henry, and A. J. B. Tolhurst, Phys. Rev. B **75**, 184308 (2007).

[69] V. B. Mikhailik, H. Kraus, D. Wahl, M. Itoh, M. Koike, and I. K. Bailiff, Phys. Rev. B **69**, 205110 (2004).

[70] R. M. Clegg, in T. Gadella, editor, *Fret and Flim Techniques*, volume 33 of *Laboratory Techniques in Biochemistry and Molecular Biology*, pages 1 – 57, Elsevier (2009), doi:http://dx.doi.org/10.1016/S0075-7535(08)00001-6.

[71] R. Lacomba-Perales, D. Errandonea, A. Segura, J. Ruiz-Fuertes, P. Rodríguez-Hernández, S. Radescu, J. López-Solano, A. Mujica, and A. Muñoz, J. Appl. Phys. **110**, 043703 (2011).

[72] N. Marzari and D. Vanderbilt, Phys. Rev. B **56**, 12847 (1997).

[73] I. Souza, N. Marzari, and D. Vanderbilt, Phys. Rev. B **65**, 035109 (2001).

[74] X. Gonze *et al.*, Comput. Phys. Comm. **180**, 2582 (2009).

[75] P. E. Blöchl, Phys. Rev. B **50**, 17953 (1994).

[76] J. P. Perdew, A. Ruzsinszky, G. I. Csonka, O. A. Vydrov, G. E. Scuseria, L. A. Constantin, X. Zhou, and K. Burke, Phys. Rev. Lett. **100**, 136406 (2008).

[77] M. Tyagi, S. Singh, A. Chauhan, and S. Gadkari, Physica B **405**, 4530 (2010).

[78] http://physics.nist.gov/PhysRefData/Star/Text/ESTAR-u.html (2012).

[79] R. Gómez-Abal, X. Li, M. Scheffler, and C. Ambrosch-Draxlfler, Phys. Rev. Lett. **101**, 106404 (2008).

[80] R. Laasner, J. Phys.: Condens. Matter. **26**, 125503 (2014).

[81] M. Daturi, M. M. Borel, A. Leclaire, L. Savary, G. Costentin, J. C. Lavalley, and B. Raveau, J. Chim. Phys. **93**, 2043 (1996).

[82] J. C. Slater and G. F. Koster, Phys. Rev. B **94**, 1498 (1954).

[83] A. A. Mostofi, J. R. Yates, Y.-S. Lee, I. Souza, D. Vanderbilt, and N. Marzari, Comput. Phys. Comm. **178**, 685 (2008).

[84] M. G. Brik, V. Nagirnyi, and M. Kirm, Mater. Chem. Phys. **113**, 1113 (2012).

[85] Y. C. Zhang, N. A. W. Holzwarth, R. T. Williams, and M. Nikl, in R. T. Williams and W. M. Yen, editors, *EXCON98: Proc. Int. Conf. on Excitonic Processes in Condensed Matter*, pages 420–425, The Electrochemical Society, Pennington, New Jersey (1998).

[86] M. Itoh, T. Katagiri, T. Aoki, and M. Fujita, Rad. Meas. **42**, 545 (2007).

CURRICULUM VITAE

Name: Raul Laasner
Date of Birth: 13.04.1987
Citizenship: Estonian
Contact: Ravila 14c, Tartu, 50411, Estonia, raullaasner@gmail.com
Education:
2006-2009 University of Tartu, BS in physics
2009-2011 University of Tartu, MS in physics
Professional career:
2011-2014 University of Tartu, Institute of Physics, engineer
Awards and stipends:
2009 University of Tartu, Institute of Physics student stipend
2011 University of Tartu, Institute of Physics student stipend
2013 Kristjan Jaak's program stipend to attend the 18th International Conference on Dynamical Processes in Excited States of Solids
List of publications:

1. S. Markov, V. Nagirnyi, A. N. Vasil'ev, V. Makhov, R. Laasner, S. Vielhauer, M. Kirm, R. Grigonis, and V. Sirutkaitis, "Modelling of decay kinetics of self-trapped exciton luminescence in $CdWO_4$ under femtosecond laser excitation in absorption saturation conditions", C. Eur. J. Phys. **10**, 1002 (2012)

2. R. Laasner, N. Fedorov, R. Grigonis, S. Guizard, M. Kirm, V. Makhov, S. Markov, V. Nagirnyi, V. Sirutkaitis, A. N. Vasil'ev, S. Vielhauer, and I. A. Tupitsyna, "Band tail absorption saturation in CdWO4 with 100 fs laser pulses", J. Phys.: Condens. Matter **25**, 245901 (2013)

3. R. Laasner, "G_0W_0 band structure of $CdWO_4$", J. Phys.: Condens. Matter **26**, 125503 (2014)

4. R. Laasner, V. Nagirnyi, S. Vielhauer, M. Kirm, D. Spassky, V. Sirutkaitis, R. Grigonis, and A. N. Vasil'ev, "Cation influence on exciton localization in homologue scheelites", accepted in J. Phys.: Condens. Matter (2015)

Elulookirjeldus

Nimi: Raul Laasner
Sünniaeg: 13.04.1987
Kodakondsus: Eesti
Kontakt: Ravila 14c, Tartu, 50411, Eesti, raullaasner@gmail.com
Haridus:
2006-2009 Tartu Ülikool, BS füüsikas
2009-2011 Tartu Ülikool, MS füüsikas
Professional career:
2011-2014 Tartu Ülikool, Füüsika Instituut, insener
Awards and stipends:
2009 Tartu Ülikool, Füüsika Instituudi tudengistipendium
2011 Tartu Ülikool, Füüsika Instituudi tudengistipendium
2013 Kristjan Jaagu välissõidu stipendium konverentsil 18th International Conference on Dynamical Processes in Excited States of Solids osalemiseks
Publikatsioonid:

1. S. Markov, V. Nagirnyi, A. N. Vasil’ev, V. Makhov, R. Laasner, S. Vielhauer, M. Kirm, R. Grigonis, and V. Sirutkaitis, "Modelling of decay kinetics of self-trapped exciton luminescence in $CdWO_4$ under femtosecond laser excitation in absorption saturation conditions", C. Eur. J. Phys. **10**, 1002 (2012)

2. R. Laasner, N. Fedorov, R. Grigonis, S. Guizard, M. Kirm, V. Makhov, S. Markov, V. Nagirnyi, V. Sirutkaitis, A. N. Vasil’ev, S. Vielhauer, and I. A. Tupitsyna, "Band tail absorption saturation in CdWO4 with 100 fs laser pulses", J. Phys.: Condens. Matter **25**, 245901 (2013)

3. R. Laasner, "G_0W_0 band structure of $CdWO_4$", J. Phys.: Condens. Matter **26**, 125503 (2014)

4. R. Laasner, V. Nagirnyi, S. Vielhauer, M. Kirm, D. Spassky, V. Sirutkaitis, R. Grigonis, and A. N. Vasil’ev, “Cation influence on exciton localization in homologue scheelites”, accepted in J. Phys.: Condens. Matter (2015)

DISSERTATIONES PHYSICAE UNIVERSITATIS TARTUENSIS

1. **Andrus Ausmees.** XUV-induced electron emission and electron-phonon interaction in alkali halides. Tartu, 1991.
2. **Heiki Sõnajalg.** Shaping and recalling of light pulses by optical elements based on spectral hole burning. Tartu, 1991.
3. **Sergei Savihhin.** Ultrafast dynamics of F-centers and bound excitons from picosecond spectroscopy data. Tartu, 1991.
4. **Ergo Nõmmiste.** Leelishalogeniidide röntgenelektronemissioon kiiritamisel footonitega energiaga 70–140 eV. Tartu, 1991.
5. **Margus Rätsep.** Spectral gratings and their relaxation in some low-temperature impurity-doped glasses and crystals. Tartu, 1991.
6. **Tõnu Pullerits.** Primary energy transfer in photosynthesis. Model calculations. Tartu, 1991.
7. **Olev Saks.** Attoampri diapasoonis voolude mõõtmise füüsikalised alused. Tartu, 1991.
8. **Andres Virro.** AlGaAsSb/GaSb heterostructure injection lasers. Tartu, 1991.
9. **Hans Korge.** Investigation of negative point discharge in pure nitrogen at atmospheric pressure. Tartu, 1992.
10. **Jüri Maksimov.** Nonlinear generation of laser VUV radiation for high-resolution spectroscopy. Tartu, 1992.
11. **Mark Aizengendler.** Photostimulated transformation of aggregate defects and spectral hole burning in a neutron-irradiated sapphire. Tartu, 1992.
12. **Hele Siimon.** Atomic layer molecular beam epitaxy of A^2B^6 compounds described on the basis of kinetic equations model. Tartu, 1992.
13. **Tõnu Reinot.** The kinetics of polariton luminescence, energy transfer and relaxation in anthracene. Tartu, 1992.
14. **Toomas Rõõm.** Paramagnetic H^{2-} and F^+ centers in CaO crystals: spectra, relaxation and recombination luminescence. Tallinn, 1993.
15. **Erko Jalviste.** Laser spectroscopy of some jet-cooled organic molecules. Tartu, 1993.
16. **Alvo Aabloo.** Studies of crystalline celluloses using potential energy calculations. Tartu, 1994.
17. **Peeter Paris.** Initiation of corona pulses. Tartu, 1994.
18. **Павел Рубин.** Локальные дефектные состояния в CuO_2 плоскостях высокотемпературных сверхпроводников. Тарту, 1994.
19. **Olavi Ollikainen.** Applications of persistent spectral hole burning in ultrafast optical neural networks, time-resolved spectroscopy and holographic interferometry. Tartu, 1996.
20. **Ülo Mets.** Methodological aspects of fluorescence correlation spectroscopy. Tartu, 1996.
21. **Mikhail Danilkin.** Interaction of intrinsic and impurity defects in CaS:Eu luminophors. Tartu, 1997.

22. **Ирина Кудрявцева.** Создание и стабилизация дефектов в кристаллах KBr, KCl, RbCl при облучении ВУФ-радиацией. Тарту, 1997.
23. **Andres Osvet.** Photochromic properties of radiation-induced defects in diamond. Tartu, 1998.
24. **Jüri Örd.** Classical and quantum aspects of geodesic multiplication. Tartu, 1998.
25. **Priit Sarv.** High resolution solid-state NMR studies of zeolites. Tartu, 1998.
26. **Сергей Долгов.** Электронные возбуждения и дефектообразование в некоторых оксидах металлов. Тарту, 1998.
27. **Kaupo Kukli.** Atomic layer deposition of artificially structured dielectric materials. Tartu, 1999.
28. **Ivo Heinmaa.** Nuclear resonance studies of local structure in $RBa_2Cu_3O_{6+x}$ compounds. Tartu, 1999.
29. **Aleksander Shelkan.** Hole states in CuO_2 planes of high temperature superconducting materials. Tartu, 1999.
30. **Dmitri Nevedrov.** Nonlinear effects in quantum lattices. Tartu, 1999.
31. **Rein Ruus.** Collapse of 3d (4f) orbitals in 2p (3d) excited configurations and its effect on the x-ray and electron spectra. Tartu, 1999.
32. **Valter Zazubovich.** Local relaxation in incommensurate and glassy solids studied by Spectral Hole Burning. Tartu, 1999.
33. **Indrek Reimand.** Picosecond dynamics of optical excitations in GaAs and other excitonic systems. Tartu, 2000.
34. **Vladimir Babin.** Spectroscopy of exciton states in some halide macro- and nanocrystals. Tartu, 2001.
35. **Toomas Plank.** Positive corona at combined DC and AC voltage. Tartu, 2001.
36. **Kristjan Leiger.** Pressure-induced effects in inhomogeneous spectra of doped solids. Tartu, 2002.
37. **Helle Kaasik.** Nonperturbative theory of multiphonon vibrational relaxation and nonradiative transitions. Tartu, 2002.
38. **Tõnu Laas.** Propagation of waves in curved spacetimes. Tartu, 2002.
39. **Rünno Lõhmus.** Application of novel hybrid methods in SPM studies of nanostructural materials. Tartu, 2002.
40. **Kaido Reivelt.** Optical implementation of propagation-invariant pulsed free-space wave fields. Tartu, 2003.
41. **Heiki Kasemägi.** The effect of nanoparticle additives on lithium-ion mobility in a polymer electrolyte. Tartu, 2003.
42. **Villu Repän.** Low current mode of negative corona. Tartu, 2004.
43. **Алексей Котлов.** Оксианионные диэлектрические кристаллы: зонная структура и электронные возбуждения. Tartu, 2004.
44. **Jaak Talts.** Continuous non-invasive blood pressure measurement: comparative and methodological studies of the differential servo-oscillometric method. Tartu, 2004.
45. **Margus Saal.** Studies of pre-big bang and braneworld cosmology. Tartu, 2004.

46. **Eduard Gerškevitš.** Dose to bone marrow and leukaemia risk in external beam radiotherapy of prostate cancer. Tartu, 2005.
47. **Sergey Shchemelyov.** Sum-frequency generation and multiphoton ionization in xenon under excitation by conical laser beams. Tartu, 2006.
48. **Valter Kiisk.** Optical investigation of metal-oxide thin films. Tartu, 2006.
49. **Jaan Aarik.** Atomic layer deposition of titanium, zirconium and hafnium dioxides: growth mechanisms and properties of thin films. Tartu, 2007.
50. **Astrid Rekker.** Colored-noise-controlled anomalous transport and phase transitions in complex systems. Tartu, 2007.
51. **Andres Punning.** Electromechanical characterization of ionic polymer-metal composite sensing actuators. Tartu, 2007.
52. **Indrek Jõgi.** Conduction mechanisms in thin atomic layer deposited films containing TiO_2. Tartu, 2007.
53. **Aleksei Krasnikov.** Luminescence and defects creation processes in lead tungstate crystals. Tartu, 2007.
54. **Küllike Rägo.** Superconducting properties of MgB_2 in a scenario with intra- and interband pairing channels. Tartu, 2008.
55. **Els Heinsalu.** Normal and anomalously slow diffusion under external fields. Tartu, 2008.
56. **Kuno Kooser.** Soft x-ray induced radiative and nonradiative core-hole decay processes in thin films and solids. Tartu, 2008.
57. **Vadim Boltrushko.** Theory of vibronic transitions with strong nonlinear vibronic interaction in solids. Tartu, 2008.
58. **Andi Hektor.** Neutrino Physics beyond the Standard Model. Tartu, 2008.
59. **Raavo Josepson.** Photoinduced field-assisted electron emission into gases. Tartu, 2008.
60. **Martti Pärs.** Study of spontaneous and photoinduced processes in molecular solids using high-resolution optical spectroscopy. Tartu, 2008.
61. **Kristjan Kannike.** Implications of neutrino masses. Tartu, 2008.
62. **Vigen Issahhanjan.** Hole and interstitial centres in radiation-resistant MgO single crystals. Tartu, 2008.
63. **Veera Krasnenko.** Computational modeling of fluorescent proteins. Tartu, 2008.
64. **Mait Müntel.** Detection of doubly charged higgs boson in the CMS detector. Tartu, 2008.
65. **Kalle Kepler.** Optimisation of patient doses and image quality in diagnostic radiology. Tartu, 2009.
66. **Jüri Raud.** Study of negative glow and positive column regions of capillary HF discharge. Tartu, 2009.
67. **Sven Lange.** Spectroscopic and phase-stabilisation properties of pure and rare-earth ions activated ZrO_2 and HfO_2. Tartu, 2010.
68. **Aarne Kasikov.** Optical characterization of inhomogeneous thin films. Tartu, 2010.

69. **Heli Valtna-Lukner.** Superluminally propagating localized optical pulses. Tartu, 2010.
70. **Artjom Vargunin.** Stochastic and deterministic features of ordering in the systems with a phase transition. Tartu, 2010.
71. **Hannes Liivat.** Probing new physics in e+e− annihilations into heavy particles via spin orientation effects. Tartu, 2010.
72. **Tanel Mullari.** On the second order relativistic deviation equation and its applications. Tartu, 2010.
73. **Aleksandr Lissovski.** Pulsed high-pressure discharge in argon: spectroscopic diagnostics, modeling and development. Tartu, 2010.
74. **Aile Tamm.** Atomic layer deposition of high-permittivity insulators from cyclopentadienyl-based precursors. Tartu, 2010.
75. **Janek Uin.** Electrical separation for generating standard aerosols in a wide particle size range. Tartu, 2011.
76. **Svetlana Ganina.** Hajusandmetega ülesanded kui üks võimalus füüsikaõppe efektiivsuse tõstmiseks. Tartu, 2011
77. **Joel Kuusk.** Measurement of top-of-canopy spectral reflectance of forests for developing vegetation radiative transfer models. Tartu, 2011.
78. **Raul Rammula**. Atomic layer deposition of HfO_2 – nucleation, growth and structure development of thin films. Tartu, 2011.
79. **Сергей Наконечный.** Исследование электронно-дырочных и интерстициал-вакансионных процессов в монокристаллах MgO и LiF методами термоактивационной спектроскопии. Тарту, 2011.
80. **Niina Voropajeva.** Elementary excitations near the boundary of a strongly correlated crystal. Tartu, 2011.
81. **Martin Timusk.** Development and characterization of hybrid electro-optical materials. Tartu, 2012, 106 p.
82. **Merle Lust.** Assessment of dose components to Estonian population. Tartu, 2012, 84 p.
83. **Karl Kruusamäe.** Deformation-dependent electrode impedance of ionic electromechanically active polymers. Tartu, 2012, 128 p.
84. **Liis Rebane.** Measurement of the $W \to \tau\nu$ cross section and a search for a doubly charged Higgs boson decaying to τ-leptons with the CMS detector. Tartu, 2012, 156 p.
85. **Jevgeni Šablonin.** Processes of structural defect creation in pure and doped MgO and NaCl single crystals under condition of low or super high density of electronic excitations. Tartu, 2013, 145 p.
86. **Riho Vendt**. Combined method for establishment and dissemination of the international temperature scale. Tartu, 2013, 108 p.
87. **Peeter Piksarv.** Spatiotemporal characterization of diffractive and non-diffractive light pulses. Tartu, 2013, 156 p.
88. **Anna Šugai.** Creation of structural defects under superhigh-dense irradiation of wide-gap metal oxides. Tartu, 2013, 108 p.

89. **Ivar Kuusik.** Soft X-ray spectroscopy of insulators. Tartu, 2013, 113 p.
90. **Viktor Vabson**. Measurement uncertainty in Estonian Standard Laboratory for Mass. Tartu, 2013, 134 p.
91. **Kaupo Voormansik.** X-band synthetic aperture radar applications for environmental monitoring. Tartu, 2014, 117 p.
92. **Deivid Pugal.** hp-FEM model of IPMC deformation. Tartu, 2014, 143 p.
93. **Siim Pikker.** Modification in the emission and spectral shape of photostable fluorophores by nanometallic structures. Tartu, 2014, 98 p.
94. **Mihkel Pajusalu**. Localized Photosynthetic Excitons. Tartu, 2014, 183 p.
95. **Taavi Vaikjärv.** Consideration of non-adiabaticity of the Pseudo-Jahn-Teller effect: contribution of phonons. Tartu, 2014, 129 p.
96. **Martin Vilbaste.** Uncertainty sources and analysis methods in realizing SI units of air humidity in Estonia. Tartu, 2014, 111 p.
97. **Mihkel Rähn.** Experimental nanophotonics: single-photon sources- and nanofiber-related studies. Tartu, 2015, 107 p.